



Characterization of the Ejecta from the NASA/DART Impact on Dimorphos: Observations and Monte Carlo Models

Fernando Moreno¹ , Adriano Campo Bagatin^{2,3}, Gonzalo Tancredi⁴ , Jian-Yang Li⁵, Alessandro Rossi⁶ , Fabio Ferrari⁷ , Masatoshi Hirabayashi⁸ , Eugene Fahnestock⁹, Alain Maury¹⁰, Robert Sandness¹⁰, Andrew S. Rivkin¹¹ , Andy Cheng¹¹, Tony L. Farnham¹² , Stefania Soldini¹³, Carmine Giordano⁷, Gianmario Merisio⁷, Paolo Panicucci⁷, Mattia Pugliatti⁷, Alberto J. Castro-Tirado^{1,14}, Emilio Fernández-García¹, Ignacio Pérez-García¹, Stavro Ivanovski¹⁵, Antti Penttilä¹⁶, Ludmilla Kolokolova¹⁷ , Javier Licandro^{18,19} , Olga Muñoz¹, Zuri Gray^{20,21}, Jose L. Ortiz¹ , and Zhong-Yi Lin²²

¹Instituto de Astrofísica de Andalucía, CSIC Glorieta de la Astronomía, s/n, E-18008 Granada, Spain

²Instituto de Física Aplicada a las Ciencias y las Tecnologías (IUFACyT), Universidad de Alicante, San Vicent del Raspeig, E-03690 Alicante, Spain

³Departamento de Física, Ingeniería de Sistemas y Teoría de la Señal Universidad de Alicante, San Vicent del Raspeig, E-03690 Alicante, Spain

⁴Departamento de Astronomía, Facultad de Ciencias, Iguá 4225, 11400 Montevideo, Uruguay

⁵Planetary Science Institute, Tucson, AZ, USA

⁶FAC-CNR, Via Madonna del Piano 10, I-50142, Sesto Fiorentino, Italy

⁷Department of Aerospace Science and Technology, Politecnico di Milano, Milano, Italy

⁸Auburn University, Auburn, AL, USA

⁹Jet Propulsion Laboratory, California Institute of Technology, Pasadena, CA, USA

¹⁰SPACEOBS, San Pedro de Atacama, Chile

¹¹Johns Hopkins University Applied Physics Laboratory, Laurel, MD, USA

¹²University of Maryland, Department of Astronomy, College Park, MD, USA

¹³Department of Mechanical, Materials and Aerospace Engineering, University of Liverpool, Liverpool, UK

¹⁴Unidad Asociada al CSIC, Departamento de Ingeniería de Sistemas y Automática, Escuela de Ingenierías, Universidad de Málaga, Málaga, Spain

¹⁵INAF—Osservatorio Astronomico di Trieste, Via G.B. Tiepolo, 11, Trieste, Italy

¹⁶Department of Physics, P.O. Box 64, FI-00014, University of Helsinki, Finland

¹⁷Department of Astronomy, University of Maryland, College Park, MD, USA

¹⁸Instituto de Astrofísica de Canarias C/Vía Láctea s/n, E-38205 La Laguna, Spain

¹⁹Departamento de Astrofísica, Universidad de La Laguna, E-38206 La Laguna, Tenerife, Spain

²⁰Armagh Observatory & Planetarium, College Hill, Armagh, BT61 9DG, UK

²¹Mullard Space Science Laboratory, Department of Space and Climate Physics, University College London, Holmbury St. Mary, Dorking, Surrey RH5 6NT, UK

²²Institute of Astronomy, National Central University, No. 300, Zhongda Road, Zhongli Dist., Taoyuan City 32001, Taiwan

Received 2023 June 2; revised 2023 July 7; accepted 2023 July 16; published 2023 August 7

Abstract

The NASA Double Asteroid Redirection Test (DART) spacecraft successfully crashed on Dimorphos, the secondary component of the binary (65803) Didymos system. Following the impact, a large dust cloud was released, and a long-lasting dust tail developed. We have extensively monitored the dust tail from the ground and the Hubble Space Telescope. We provide a characterization of the ejecta dust properties, i.e., particle size distribution and ejection speeds, ejection geometric parameters, and mass, by combining both observational data sets and using Monte Carlo models of the observed dust tail. The size distribution function that best fits the imaging data is a broken power law having a power index of -2.5 for particles of $r \leq 3$ mm and -3.7 for larger particles. The particles range in size from $1 \mu\text{m}$ up to 5 cm. The ejecta is characterized by two components, depending on velocity and ejection direction. The northern component of the double tail, observed since 2022 October 8, might be associated with a secondary ejection event from impacting debris on Didymos, although it is also possible that this feature results from the binary system dynamics alone. The lower limit to the total dust mass ejected is estimated at $\sim 6 \times 10^6$ kg, half of this mass being ejected to interplanetary space.

Unified Astronomy Thesaurus concepts: Asteroid dynamics (2210)

1. Introduction

The Double Asteroid Redirection Test (DART) is a NASA mission that impacted a spacecraft on the surface of Dimorphos, the satellite of the primary asteroid (65803) Didymos (Cheng et al. 2018). On 2022 September 26, 23:14 UT, DART impacted in a nearly head-on configuration on Dimorphos's surface, giving rise to a fast ejected material (plume; speed of $\approx 2 \text{ km s}^{-1}$) whose spectrum consists of emission lines of ionized alkali metals (Na I, K I, and Li I; Shestakova et al. 2023). This plume was clearly observed in

images obtained from Les Makes Observatory (Graykowski et al. 2023) right after impact time and was also seen in the earliest images during the Hubble Space Telescope (HST) monitoring (Li et al. 2023). A wide ejection cone of dust particles and meter-sized boulders was monitored by the Light Italian CubeSat for Imaging of Asteroid (LICIAcube; Dotto et al. 2021; Farnham et al. 2023), which performed a fast flyby of the system.

Apart from the plume, a fraction of the ejected mass was emitted at significantly lower speeds, forming the ejecta pattern and tail that could be seen on the earliest images acquired from ground-based observatories (Bagnulo et al. 2023; Opitom et al. 2023) and the HST (Li et al. 2023). Our purpose is to characterize the dust properties of this mostly slow-moving ejecta, the ejection velocities, the size distribution, and the

Table 1
Technical Data of the Instrumentation Used

Telescope	Location (Latitude; Longitude)	CCD	Camera Field of View	Plate Scale (arcsec pixel ⁻¹)	Filter
HST	...	Marconi	160" × 160"	0.04	F350LP
SPACEOBS	22°57'09"8S; 68°10'48"7W	ZWO ASI6200MM Pro	49' × 29'	0.54	Clear
BOOTES	37°05'58"2N; 06°44'14"9W	Andor iXon EMCCD	16'8 × 16'8	1.97	Clear

ejected mass using Monte Carlo models to simulate the motion of the particles in the spatial region near the binary system. After describing the ejecta observations in Section 2, in Section 3, we introduce the Monte Carlo models used to calculate the synthetic tail brightness and their time evolution and discuss the results obtained. In Section 4, we provide a comparison of the DART results with those obtained from the observation of natural active asteroids. Finally, the conclusions are given in Section 5.

2. Observations

We first describe the observational material acquired from the ground, followed by a brief description of the HST observations (Li et al. 2023). Table 1 summarizes the technical data of the instrumentation used.

Aperture photometry of the binary system was performed using the BOOTES-1 telescope. The Burst Observer and Optical Transient Exploring System (BOOTES) is a worldwide robotic telescope network primarily designed to detect and follow gamma-ray bursts (Castro-Tirado et al. 2012; Hu et al. 2023). The aperture photometry measurements were performed using BOOTES-1, which is a 0.3 m aperture telescope located in the Estación de Sondeos Atmosféricos in the Centro de Experimentación, El Arenosillo, Huelva, Spain. The aperture size was selected automatically in the range 6"–7", depending on the seeing conditions. The photometric data were calibrated using standard stars in the Gaia *G*-band system (Weiler 2018).

The ground-based images were acquired from a private observatory located in the Atacama desert (Chile) called San Pedro de Atacama Celestial Explorations (SPACEOBS), which is run by Alain Maury. The Atacama desert is an excellent place for astronomical observations, with low humidity and good transparency and seeing conditions. All of the observations were performed with a CCD camera mounted on a 0.43 m aperture telescope. The technical information on the instrumentation used is displayed in Table 1. Images were acquired from the impact date (2022 September 26) to late 2022 December on 56 epochs in total. The images were acquired using a nonsidereal tracking mode, i.e., by tracking on the binary system, always using an exposure time of 300 s. The reduction of the images was performed by standard techniques, including bias subtraction and flat-fielding. The sky background was estimated in each image by taking a median value of field star-free regions in each frame. A median image was obtained on each night by stacking up all of the available reduced images. The images were calibrated to magnitudes arcsec⁻² using the photometric data from BOOTES-1 until 2022 October 20. At later epochs, we assumed for calibration of the images the *V*-band magnitude values obtained from the JPL-Horizons web interface²⁴ for the Didymos system, as the tail contribution is essentially negligible on those dates. This

involves the assumption that the “naked” system has not experienced any brightness variation from post- to preimpact conditions, which is confirmed by other observations. Thus, photometric measurements by P. Pravec et al. (2023, private communication) reveal a difference of just -0.061 mag between the pre- and postimpact absolute magnitudes, which has been detected only at the 1.9σ level (formal errors), so it is only a marginal detection of the binary system’s brightening and not statistically significant. In line with this, B. Buratti et al. (2023, personal communication) did not report any significant brightness variation in the system postimpact either, the difference being only -0.13 absolute mag relative to the preimpact data.

From the large observational data set, we selected for modeling those shown in Figure 1, whose observational parameters are given in Table 2. The earliest images acquired only 1 or 2 days after the impact already show a complex morphology, where, in addition to other smaller-scale features, two conspicuous features directed toward the north and southeast (the ejecta cone features in Figure 2, upper panel) became apparent, as well as a well-developed tail in the antisolar direction. In addition, a secondary tail appeared north of the main tail about 6 days after the impact, forming a double tail feature that is barely seen in the ground-based images (see Figures 8 and 9) but clearly seen in the HST images (see Figure 2, lower panel; see also Li et al. 2023). The origin of the northern component of the double tail is still unclear, but it clearly follows the corresponding synchrone at $T_0 + 6 \pm 1$ day (where T_0 is the impact time; Li et al. 2023).

The HST images, already described in Li et al. (2023), were acquired using the 2.4 m diameter HST with the Wide Field Camera 3 (WFC3). Additional technical details of the instrumentation used are provided in Table 1. We have selected for modeling a subset of the HST calibrated images as shown in Table 3. Images coded as (l) and (o) are depicted in Figure 2, showing the most conspicuous features observed in the images and providing a nomenclature reference.

In order to refer all of the aperture photometry data and images to a common photometric system, the solar spectrum in combination with the reflectance spectrum of the binary system should be taken into account. The output of our Monte Carlo codes is given in solar disk intensity units (i/i_\odot) that we converted to r' Sloan mag arcsec⁻², m , to compare with the observations according to the equation

$$m = 2.5 \log_{10} \Omega + m_\odot - 2.5 \log_{10}(i/i_\odot), \quad (1)$$

where Ω is the solid angle subtended by the Sun at 1 au expressed in arcsec² ($\Omega = 2.893 \times 10^6$ arcsec²), and m_\odot is the magnitude of the Sun in the r' Sloan filter, $m_\odot = -26.95$ (Ivezić et al. 2001).

If the reflected spectrum were purely solar, the aperture photometry data, given in the *G*-band system, could be converted to r' by $r' = G + 0.066$ mag (Oszkiewicz et al. 2017). On the other hand, the conversion of magnitudes in the

²⁴ <https://ssd.jpl.nasa.gov/horizons/>

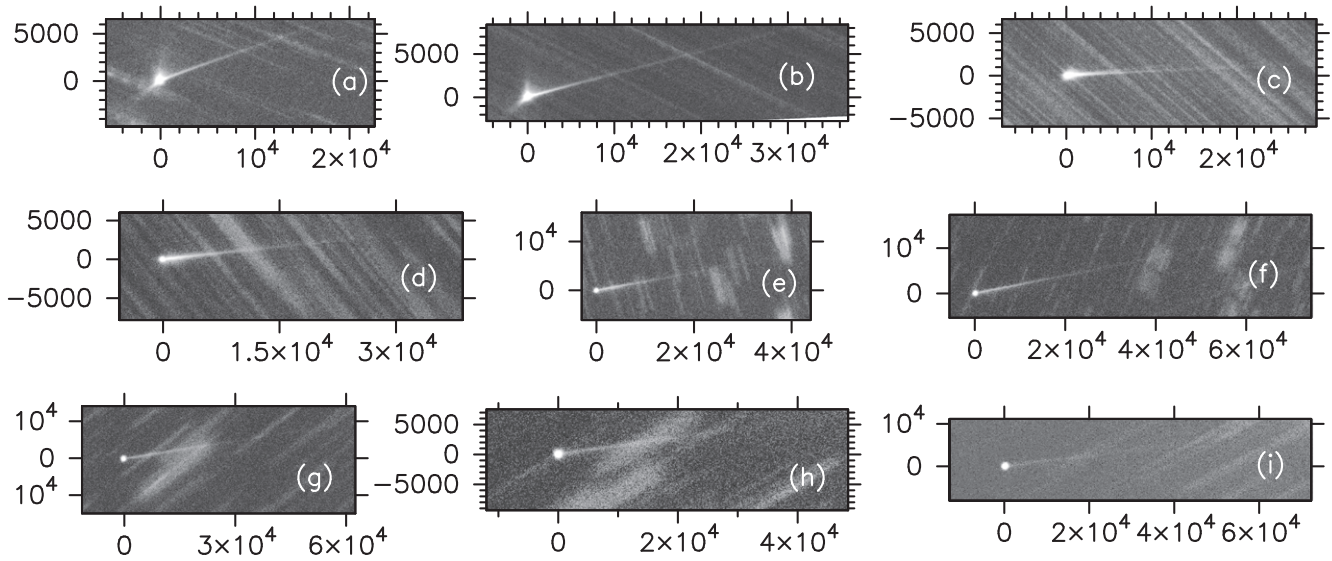


Figure 1. Subset of SPACEOBS images used for modeling. Axes are labeled in kilometers of projected distance at the asteroid in all panels. Labels (a)–(i) indicate observation time as given in Table 2. Celestial north is up, and celestial east is left in all panels.

Table 2
Log of SPACEOBS Observations

Time (UT)	Time since Impact (days)	r_h^a (au)	Δ^b (au)	PsAng ^c (deg)	PIAng ^d (deg)	α^e (deg)	Code
2022 Sep 30 07:41	3.32	1.037 8	0.072	292.45	48.67	58.24	(a)
2022 Oct 3 06:43	6.28	1.031 5	0.071	288.23	48.19	62.56	(b)
2022 Oct 16 07:12	19.30	1.014 5	0.081	280.87	34.34	75.20	(c)
2022 Nov 2 07:26	36.31	1.020 2	0.113	283.72	16.63	72.70	(d)
2022 Nov 18 08:24	52.35	1.053 3	0.147	284.81	6.80	60.31	(e)
2022 Dec 2 07:26	66.31	1.100 7	0.176	282.22	1.05	45.82	(f)
2022 Dec 17 06:00	81.25	1.165 7	0.212	273.76	−3.30	28.33	(g)
2022 Dec 22 08:10	86.34	1.190 4	0.227	268.42	−4.38	22.32	(h)
2022 Dec 24 07:13	88.30	1.200 1	0.233	265.75	−4.73	20.06	(i)

Notes.

^a Heliocentric distance.

^b Geocentric distance.

^c Position angle of the extended Sun-to-asteroid radius vector.

^d Angle between observer and asteroid orbital plane.

^e Phase angle.

HST F350LP filter to Johnson’s V has been given by Nolan et al. (2019) as $V = F_{350LP} - 0.12$ mag. Then, using the relation $r' = V - 0.49(B - V) + 0.11$ mag (Fukugita et al. 1996), valid for stars with $(B - V) \leq +1.5$ mag, and the solar color index $(B - V) = 0.629$ mag (Willmer 2018), we get $r' = F_{350LP} - 0.32$ mag. However, the reflectance spectrum of the unaltered Didymos–Dimorphos system exhibits temporal variations in slope that can be attributed to a number of things, including compositional changes on Didymos’s surface (Ieva et al. 2022), preventing us from performing any precise photometric correction. In addition, the spectrum of the freshly ejected material after the DART collision might be spectroscopically different as well. Then, we decided to maintain all of the measurements in their original units. In any case, based on the given color index conversion assuming a solar-like spectrum, we do not expect variations higher than ≈ 0.3 mag among the different bands (Gaia G and F350LP) and the r' Sloan magnitudes.

3. Dust Tail Modeling

Our purpose is to perform an interpretation of the available observed images with Monte Carlo techniques, i.e., by direct calculation of the orbits of the individual particles ejected at the time of impact, and the computation of their positions in space at the time of the observation.

To calculate the orbits of the ejected dust particles, we used two different approaches. The first one, which we call simple Monte Carlo modeling, assumes that the particles are initially placed out of the Hill sphere of the system, where the gravity of the binary components can be neglected, and then the dust grains are influenced by solar gravity and radiation pressure forces only. In consequence, the particles undergo purely Keplerian orbits around the Sun, and their orbits can be easily integrated. This approach is adequate to describe the escaping ejecta and suited to analyze the large-scale, low-resolution, ground-based SPACEOBS observations. The second approach, which we call detailed Monte Carlo modeling, is used to

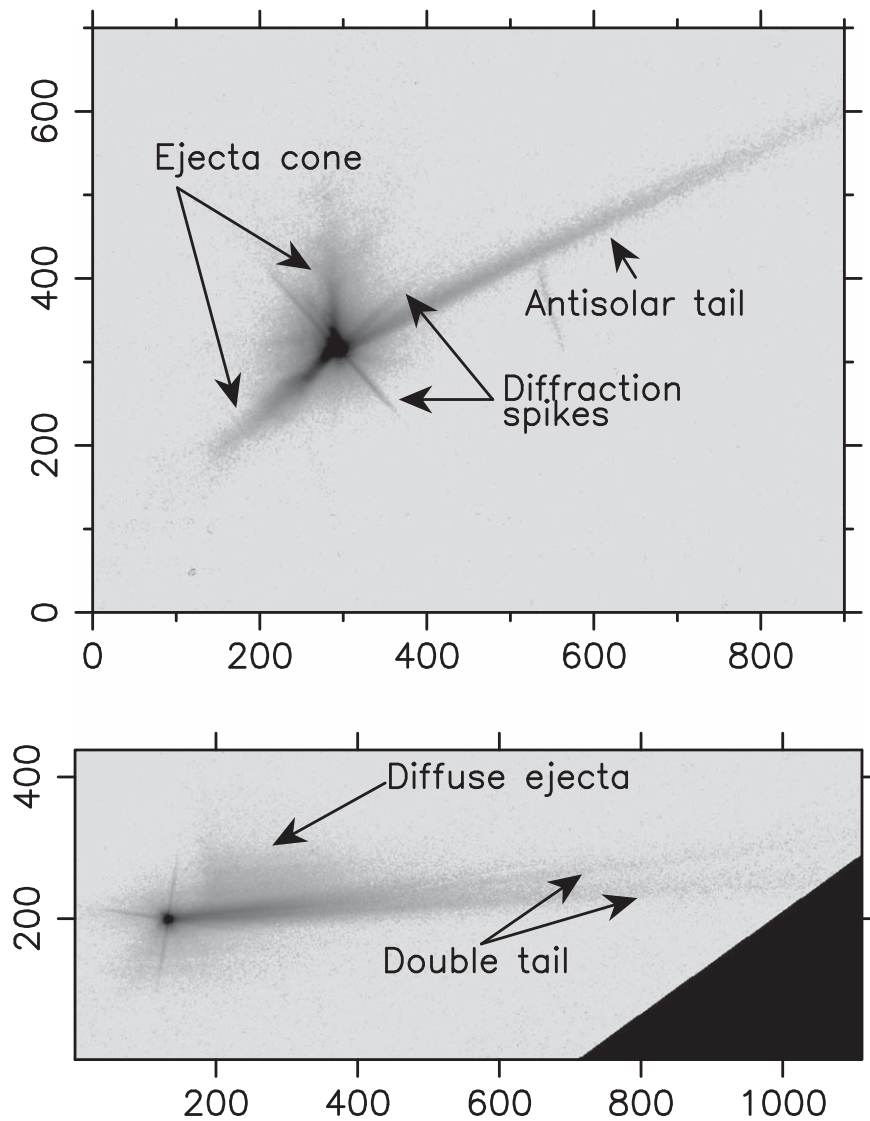


Figure 2. The HST images obtained on 2022 September 28 (code (l); upper panel) and 2022 October 8 (code (o)) in Table 3, indicating the most obvious features encountered in the images. Axes are labeled in pixels, where 1 pixel represents ≈ 2 km projected on the sky. Celestial north is up, and celestial east is left in both panels.

Table 3
Log of the HST Observations

Time (UT)	Time since Impact (days)	r_h (au)	Δ (au)	PsAng (deg)	PIAng (deg)	α (deg)	Code
2022 Sep 27 01:04	0.04	1.046	0.076	297.84	47.59	53.34	(j)
2022 Sep 27 07:25	0.31	1.045	0.075	297.39	47.73	53.74	(k)
2022 Sep 28 02:28	1.10	1.043	0.074	296.05	48.11	54.92	(l)
2022 Oct 1 16:12	4.67	1.035	0.072	290.42	48.63	60.25	(m)
2022 Oct 5 18:38	8.78	1.027	0.071	285.41	46.68	65.94	(n)
2022 Oct 8 19:40	11.82	1.022	0.073	282.95	43.76	69.56	(o)
2022 Oct 11 20:42	14.86	1.018	0.075	281.53	40.10	72.44	(p)
2022 Oct 15 10:26	18.43	1.015	0.078	280.90	35.46	74.80	(q)

describe the dynamics in the innermost region close to the binary system and is based on the integration of the equations of motion of the particles, taking the gravitational fields of the two bodies fully into account. Owing to the superb spatial resolution of the HST images, this approach is better suited to analyze the details of the features that appear in those images but has the obvious drawback of the large CPU time needed to

run the model in comparison with the simple Monte Carlo model.

After setting the particle scattering properties, particularly the geometric albedo, the results of the models (i.e., the evolution of the tail brightness with time) depend on three basic parameters: the ejection velocities, the size distribution, and the total dust mass ejected after the DART impact. The combination of those

parameters affects the tail brightness in an intricate manner. Thus, small dust particles are highly affected by radiation pressure and quickly populate the far tail regions, while larger particles need a much longer time to leave the near-nucleus²⁵ region, depending on ejection speed. In addition, in the detailed model calculations, those particles might be trapped for a long time, orbiting close to the binary system and leaking out from it very slowly, especially if the ejection speeds are close to the escape velocity of Dimorphos. High ejection speeds spread out the particles quickly, so that the tail brightness will tend to decrease. The size distribution, which is commonly set to a power-law function, defines the range of sizes that dominate the total mass. Thus, for power exponents lower than -4 , most of the mass would be concentrated in the smallest particles, while for exponents higher than -3 , most of the mass would reside on the larger ones.

The fitting procedure is based on selecting upper and lower limits to the parameter inputs and experimenting with them until a reasonable agreement with all of the observations is achieved. Due to the many parameters involved, we cannot ensure that the best-fitting parameters constitute the only solution to the problem. The main weakness of the modeling resides in the difficulty of constraining the total mass ejected, on one hand because of the presence in the particle population of meter-sized and larger boulders that mostly contribute to the mass but not the brightness when compared with the much more abundant small particle population, and, on the other hand, because of the very high-speed ejecta (see, e.g., Fitzsimmons et al. 2023) immediately after impact, which leaves the field of view of the cameras in a very short time interval. We will come back to these problems in the next section.

3.1. Simple Monte Carlo Modeling

The interpretation of the ground-based dust tail brightness in terms of the simple dynamical-radiative models is made using our Monte Carlo model as described in, e.g., Moreno et al. (2022a, and references therein). In such an approach, as stated above, the particles are assumed to be affected by the solar gravity and radiation pressure only, ignoring the gravity perturbations of the two components of the binary system. Then, this model is valid out of the Hill sphere of the system; i.e., it is useful to characterize the material that has gravitationally escaped from the binary system but cannot be used to describe the complex dynamics in the vicinity of the asteroid pair. In fact, we will see with the detailed Monte Carlo model that a significant fraction of the ejected mass is lost in collisions with either Didymos or Dimorphos, thus reducing the dust mass ejected to interplanetary space.

In the simulations, a large number ($\gtrsim 10^7$) of particles are released with a certain velocity distribution and particle size distribution. The total ejected mass must also be specified. For this application of the code, all of the particles are assumed to be ejected instantly, except for a secondary ejection event occurring a few days after the impact, which explains the development of an additional tail component forming a small angle toward north of the main tail, to be described at the end of this section. The particles are considered spherical, independent scatterers, and they do not experience collisions

among them or disruption or fragmentation phenomena. Their dynamics is governed by the so-called β parameter (not to be confused with the momentum transfer efficiency due to the DART impact, usually also denoted by β), defined as the ratio of solar radiation pressure force to solar gravity force, as $\beta = F_{\text{rad}}/F_{\text{grav}} = C_{\text{pr}}Q_{\text{pr}}/(2\rho_p r)$. In that equation, r is the particle radius, ρ_p is its density (assumed at 3500 kg m^{-3}), $C_{\text{pr}} = 1.19 \times 10^{-3} \text{ kg m}^{-2}$ is the radiation pressure constant, and Q_{pr} is the scattering efficiency for radiation pressure, which becomes $Q_{\text{pr}} \approx 1$ for moderately absorbing particles with $r \gtrsim 1 \mu\text{m}$ (see, e.g., Moreno et al. 2012, their Figure 5). The assumed density of $\rho_p = 3500 \text{ kg m}^{-3}$ corresponds to the density of ordinary chondrite meteorites associated with the S-type spectrum exhibited by the Didymos–Dimorphos system (Dunn et al. 2013). All particles are assumed to have the same density. The Keplerian trajectories of the particles can be determined from their β parameter and the ejection velocity vector. At the end of the integration time, their positions on the sky plane at any time after ejection are recorded. The brightness contribution of each particle in a given pixel of the synthetic image, m , expressed in mag arcsec^{-2} , is given by

$$p_R \pi r^2 = \frac{2.24 \times 10^{22} \pi r_h^2 \Delta^2 10^{0.4(m_\odot - m)}}{G(\alpha)}, \quad (2)$$

where r_h is the asteroid heliocentric distance in au, Δ is the geocentric distance of the asteroid, and m_\odot is the apparent solar magnitude in the appropriate passband. The particle’s geometric albedo at zero phase angle is given by p_R , and $G(\alpha) = 10^{-0.4\alpha\phi}$ is the phase correction, where α is the phase angle, and ϕ is the linear phase coefficient. Recent work by Lolachi et al. (2023), however, shows the calculated geometric albedo dependence with phase angle, revealing values between 0.07 and 0.15 for p_R for a range of particle sizes, compositions, and different porosities from several sources, including laboratory data by Muñoz et al. (2020) and emitted particles from asteroid Bennu (Hergenrother et al. 2020), for phase angles smaller than about 60° , so that we adopted $p_R = 0.1$ and $G(\alpha) = 1$. In any case, in the geometric optics approximation, which holds for the derived size distribution functions, the ejected mass is directly proportional to the geometric albedo, so that for higher albedos, the dust mass ejected will be lower accordingly. In the vicinity of the image optocenters, the contribution of the nucleus reflected light (i.e., the scattered light of the spherical body having an equivalent radius to the Didymos+Dimorphos system) is important, as it may be comparable to or higher than the dust cloud brightness. In fact, for images taken a few weeks after impact, the contribution of the nucleus brightness to the total brightness is dominant. The equivalent radius of the system can be approximately computed as an average of the Didymos radius and the effective radius of the Didymos+Dimorphos system, which turns out to be $R_n = 395 \text{ m}$, i.e., only a bit higher than Didymos’s radius, as it has a much larger surface than Dimorphos. Then, to compute the contribution of the nucleus, we assume a spherical body with the same value of geometric albedo given above for the particles. Following the magnitude–phase relationship by Shevchenko (1997), for $p_R = 0.1$, we get $\phi = 0.013 - 0.0104 \ln p_R = 0.037 \text{ mag deg}^{-1}$. This value is very close to that obtained by B. Buratti et al. (2023, personal communication) of $\phi = 0.035 \pm 0.001 \text{ mag deg}^{-1}$.

²⁵ In the context of this paper, we always refer to the “nucleus” as to the two asteroids of the binary system that are seen as an effective single body in the comet-like appearance in the Earth-based telescope images of the ejecta.

The ejection of material is mainly modeled by two ejecta components traveling at different speeds. This is justified below in order to reproduce both the antisolar tail (slow-speed component) and the conical features (high-speed component). This component, which contributes one-third of the total ejected mass, is assumed to be characterized by a hollow conical shape whose axis is oriented to the equatorial coordinates R.A. = 130° , decl. = 17° , which is within the range of the current determinations. The impactor direction was R.A. = 128° , decl. = 18° (e.g., Hirabayashi et al. 2023). Recent detailed calculations of the ejecta geometry by Hirabayashi et al. (2023) predict an emission cone elongated along the north–south direction of Dimorphos with the cone axis oriented to R.A. = $140^\circ \pm 4^\circ$, decl. = $17^\circ \pm 7^\circ$ (the uncertainties are 1σ values). However, the precise axis direction does not have a significant impact on the results as long as it does not deviate by more than 10° from the assumed direction. The cone aperture is set to 140° , and the cone wall thickness is set to 10° . The second ejecta component is described by a hemispherical ejection with the same axis as the conical emission and contributing two-thirds of the ejected mass.

The remaining model parameters are the size distribution and the initial speeds. The size distribution function is initially set to a single differential power-law distribution function with power exponent κ , i.e., $dn \propto r^\kappa dr$, where dn is the number of particles between r and $r + dr$. We assumed an initial value for κ of $\kappa = -2.5$, close to the value obtained by Li et al. (2023) on the earliest HST images. The size distribution was assumed to be the same for all of the ejecta components.

Concerning ejection velocities, conventional scaling laws for cratering ejecta generally refer to velocity distributions as a function of launch position (e.g., Housen et al. 1983; Cintala et al. 1999; Housen & Holsapple 2011) and do not include the effects of the different sizes of the particles populating the distribution. Only a few experimental or observational studies provide information on velocity distribution as a function of grain size, but in all cases, because of technical limitations, they refer to sizes in the millimeter range and larger, up to boulder-sized debris (e.g., Okawa et al. 2022). After repeated experimentation with the model, it soon became apparent that a double component was needed for the ejecta speeds—one component associated with faster particles giving rise to the two features associated with the conical ejection (high-speed component) and another with ejection velocities close to Dimorphos’s escape velocity (slow-speed component)—to properly model the length and thickness of the antisolar tail (the hemispherical ejecta component). The faster ejecta was modeled following a power-law function of the particle size, as it has been set to model the ejection speeds for natural impacts on asteroids (596) Scheila (Ishiguro et al. 2011) and 354P/LINEAR (Kleyna et al. 2013; Kim et al. 2017). On the other hand, the velocities of the slow-speed component are modeled as $v = 0.05(1 + \chi) \text{ m s}^{-1}$, where χ is a random number in the (0, 1) interval. The randomization in the speed distribution is imposed in an attempt to somehow mimic its stochastic nature. The high-speed ejecta was modeled by $v = 0.375\chi r^{-0.5} \text{ m s}^{-1}$ (with r expressed in meters). Ejecta speed estimates of $\sim 2 \text{ m s}^{-1}$ for millimeter-sized particles have been reported by Roth et al. (2023) from ALMA observations of the DART impact. This is in line with our average higher-speed ejecta estimates of $\sim 6 \text{ m s}^{-1}$ for $r = 1 \text{ mm}$ particles. As stated above, the reason for a double ejecta component is

motivated by the appearance of the conical feature in combination with the antisolar tail; this tail cannot be modeled assuming the conical high-speed component, as it would generate a tail far broader and more diffuse than observed. The slow-speed component, which encompasses most of the ejected mass (two-thirds of the total dust mass), could be associated with the large amount of material that is ejected at a slow velocity during the latter stages of crater formation, as determined from conventional scaling laws (e.g., Housen et al. 1983). In addition, there is another mechanism that might be contributing to this slow ejecta component: the lofting of particles owing to the propagation of seismic waves after the impact (Tancredi et al. 2023).

In conjunction with the two components of the ejecta just described, a third dust ejecta emission event took place on 2022 October 2.5, leading to the secondary northern branch of the tail. This event is associated with the presence of the northern secondary tail that follows the corresponding synchronone at the given epoch. This agrees with the timing obtained by Li et al. (2023) from HST images ($T_0 + 6 \pm 1$ days). The small tail thickness suggests low ejection velocities, and its faintness compared to the main tail suggests a much smaller ejected mass than the main tail slow component of the ejecta. For simplicity, we adopt the same parameters of the slow ejecta component mentioned above (i.e., $v = 0.05(1 + \chi) \text{ m s}^{-1}$) and isotropic ejection. We will link this dust emission event to the impacts of debris particles on Didymos in the framework of the detailed Monte Carlo approach (see Section 3.2). At this point, it is interesting to note that a slight increase in brightness has been observed around 6–9 days after impact in both ground-based and HST photometric light curves (Kareta et al. 2023). This so-called “eighth-day bump” could be associated with reimpacting material on Didymos, as we will also show later in Section 3.2.

The dust masses ejected for each component that better fits the tail profiles were 2.2×10^7 (slow-speed), 7.4×10^6 (high-speed), and $3.7 \times 10^6 \text{ kg}$ (late event), respectively, giving a total mass ejected of $3.3 \times 10^7 \text{ kg}$. The mass of the secondary ejecta component is just a rough estimate; the signal-to-noise ratio of that secondary tail is too low to allow for a better constraint. This estimate will be improved with the analysis of the much higher resolution HST images (Section 3.2).

The maximum particle size in the distribution was constrained by the analysis of the latest images. Thus, the initial assumed radius $r_{\text{max}} = 1 \text{ cm}$ had to be increased to larger values. The reason is that for $r_{\text{max}} = 1 \text{ cm}$, the central condensation containing the nuclei would be detached from the tail at the latest observation dates because the radiation pressure would be moving those $r = 1 \text{ cm}$ particles away some months after impact. Then, a larger size limit of $r_{\text{max}} = 5 \text{ cm}$ was set instead, providing a better fit to the near-nucleus region. Regarding the minimum particle size, setting $r_{\text{min}} = 1 \mu\text{m}$ was found to be adequate to fit the outermost part of the tail in the earliest images. Also, as we will describe later in this section, this lower limit is very well constrained by the earliest HST images, where the observed length of the tail is very consistent with that minimum size.

With all of the above model inputs, the resulting photometric scans along the tails of the images in comparison with the observations at the dates shown in Table 2 are displayed in Figure 3. Although the fits to the early images are reasonably good, the model does not perform well for images acquired later than ≈ 10 days after impact. Varying the power index κ does not produce any improvement either. As the observed

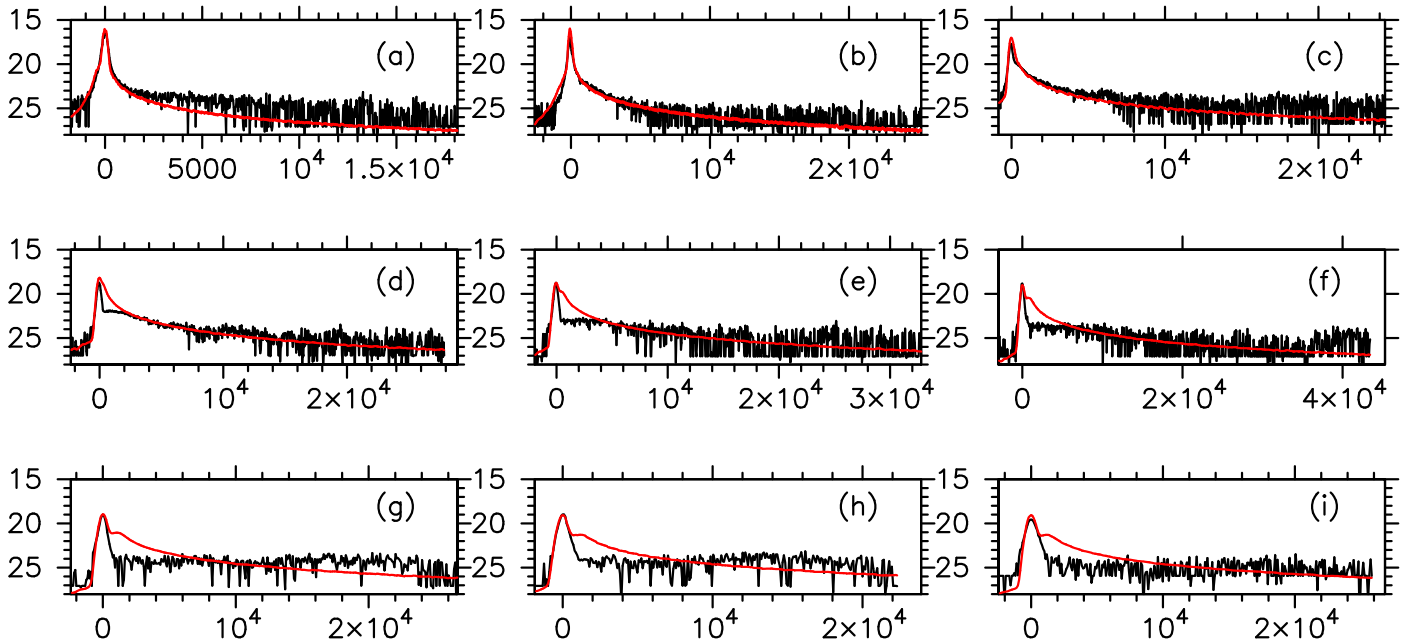


Figure 3. Scans along the tails of the SPACEOBS images. The panels are labeled (a)–(i), corresponding to the dates shown in Table 2 (“Code” column). The black lines correspond to the observations and the red line to the model. The horizontal axes are labeled in kilometers projected on the sky plane, and the vertical axes are expressed in mag arcsec^{-2} . These scans were obtained using a single power-law size distribution with $\kappa = -2.5$. The total dust mass released is 3.2×10^7 kg.

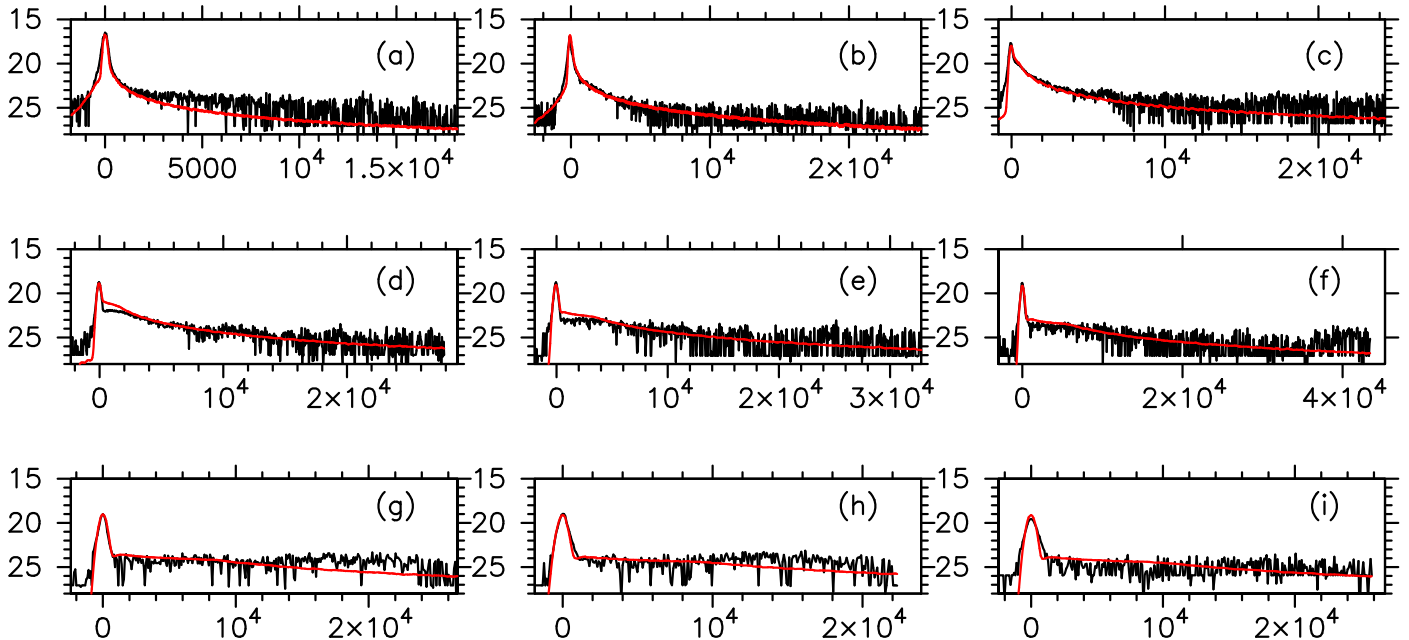


Figure 4. Scans along the tails of the SPACEOBS images. The panels are labeled (a)–(i), corresponding to the dates shown in Table 2 (“Code” column). The black lines correspond to the observations and the red line to the model. The horizontal axes are labeled in kilometers projected on the sky plane, and the vertical axes are expressed in mag arcsec^{-2} . These scans were obtained using a broken power-law differential size distribution function with $\kappa = -2.5$ between $1 \mu\text{m}$ and 3mm and $\kappa = -3.7$ between 3mm and 5cm . The total dust mass sent to interplanetary space is 4.2×10^6 kg.

brightness in the near-nucleus region is clearly overestimated with this model, we imposed a broken power law with a “knee” in the millimeter size range to search for an improvement in the fits. We found that a broken power law with $\kappa = -2.5$ for particles smaller than 3mm and a higher slope of $\kappa = -3.7$ for particles having radii larger than 3mm produces much better fits at all epochs, as can be seen in Figure 4. The assumption of a different size distribution with a higher slope on the largest particles implies a recalculation of the ejected masses that now become a factor of ≈ 8 smaller, i.e., 2.8×10^6

and 9.2×10^5 kg for the slow and fast components, respectively, and 4.6×10^5 kg for the secondary, late, ejecta, giving a total mass of 4.2×10^6 kg. It is important to realize that this dust mass constitutes a stringent lower limit to the total ejected mass from Dimorphos. On one hand, the high-speed ($\approx 2 \text{ km s}^{-1}$) material released right after the impact (see Shestakova et al. 2023) is out of the field of view on our images. On the other hand, the presence in the particle distribution of very large particles, such as boulders, might contribute significantly to the total ejected mass but very little to the brightness, becoming almost

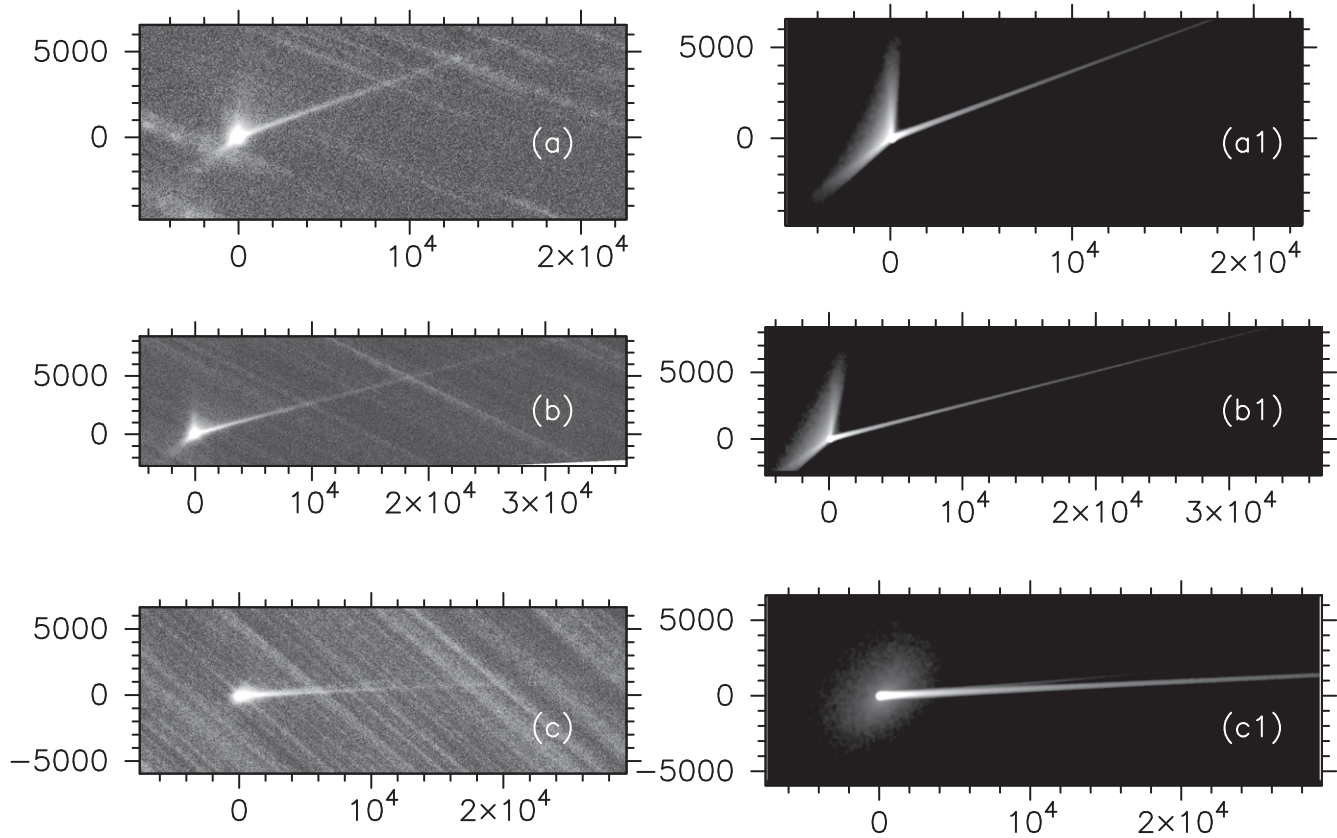


Figure 5. Panels (a), (b), and (c) display the SPACEOBS images at the corresponding dates in Table 2, and panels (a1), (b1), and (c1) display the corresponding synthetic images generated with the simple Monte Carlo model. All images are stretched between 28 and 22 mag arcsec⁻². Axes are labeled in kilometers projected on the sky plane. North is up and east is to the left in all images.

Table 4
Parameters of the Best-fit Models

Ejecta	Speed	Ejected	Ejection	Total Unbound Ejected Mass (kg)
Component	(m s ⁻¹)	Mass (kg)	Mode	
Simple Monte Carlo Model				
Slow	0.05(1 + ξ)	2.8×10^6	Hemispherical	4.2×10^6
Fast	$0.375\chi r^{-0.5}$	9.2×10^5	Conical	
Late	0.05(1 + ξ)	4.6×10^5	Isotropic	
Detailed Dynamical Monte Carlo Model				
Slow	0.09	4.3×10^6	Hemispherical	4.9×10^6
Fast	$0.225\chi r^{-0.5}$	2.1×10^6	Conical	
Late	0.09	3.0×10^6	Isotropic	

Note.

^a Delivered to interplanetary space. Note that in the case of the detailed dynamical Monte Carlo model, this mass is not the sum of the total masses ejected due to intervening dynamical stirring and collision of a sizable fraction of the ejecta with Didymos and Dimorphos.

undetectable in the images. In that respect, it is convenient to mention the findings by Farnham et al. (2023), who detected a boulder population after DART impact by analyzing LICIACube LUKE images. Those authors found a population of some 100 meter-sized boulders, so that, assuming a density of 3500 kg m⁻³, they would give a total mass of $\approx 1.5 \times 10^6$ kg. Those boulders are moving at speeds of 20–50 m s⁻¹, so that

they carry a momentum that might be comparable to that of the DART spacecraft (Farnham et al. 2023). Let us assume that the actual boulder population was a factor of 100 higher, i.e., a total mass of 10⁸ kg, and that this population is distributed following a power law of index -3.7 (as in our model) with ejection speeds of 20 m s⁻¹. This would result in a unrealistic momentum balance, but we would like to remark that even in this case, the boulder population would add a negligible increase in the integrated flux of only 0.06% relative to the corresponding model results on the dates shown in Table 2. Even if we reduce the speed of those boulders to the much smaller speeds used in the modeling (see Table 4), that will tend to concentrate the boulders much closer to the optocenter at all epochs, the contribution to the total flux coming from the boulders would be of only 7% compared with the flux computed with the best-fit model parameters.

The synthetic images generated are convolved with a Gaussian function of FWHM consistent with the average seeing point-spread function. The modeled images are then compared to the observed images in Figures 5–7 using the same gray scale. As shown, the modeled images capture well many of the features displayed in the observed images.

The model image showing the double tail in comparison with the SPACEOBS observation is given in more detail in Figure 8. For purposes of comparison only, an additional image, taken at the LULIN Observatory 1 m aperture telescope in Taiwan on October 12, i.e., 4 days before the SPACEOBS image on October 16, also displays the feature, with a slightly higher signal-to-noise ratio than the SPACEOBS image in Figure 8, see Lin et al. (2023; Figure 9). By November 2,

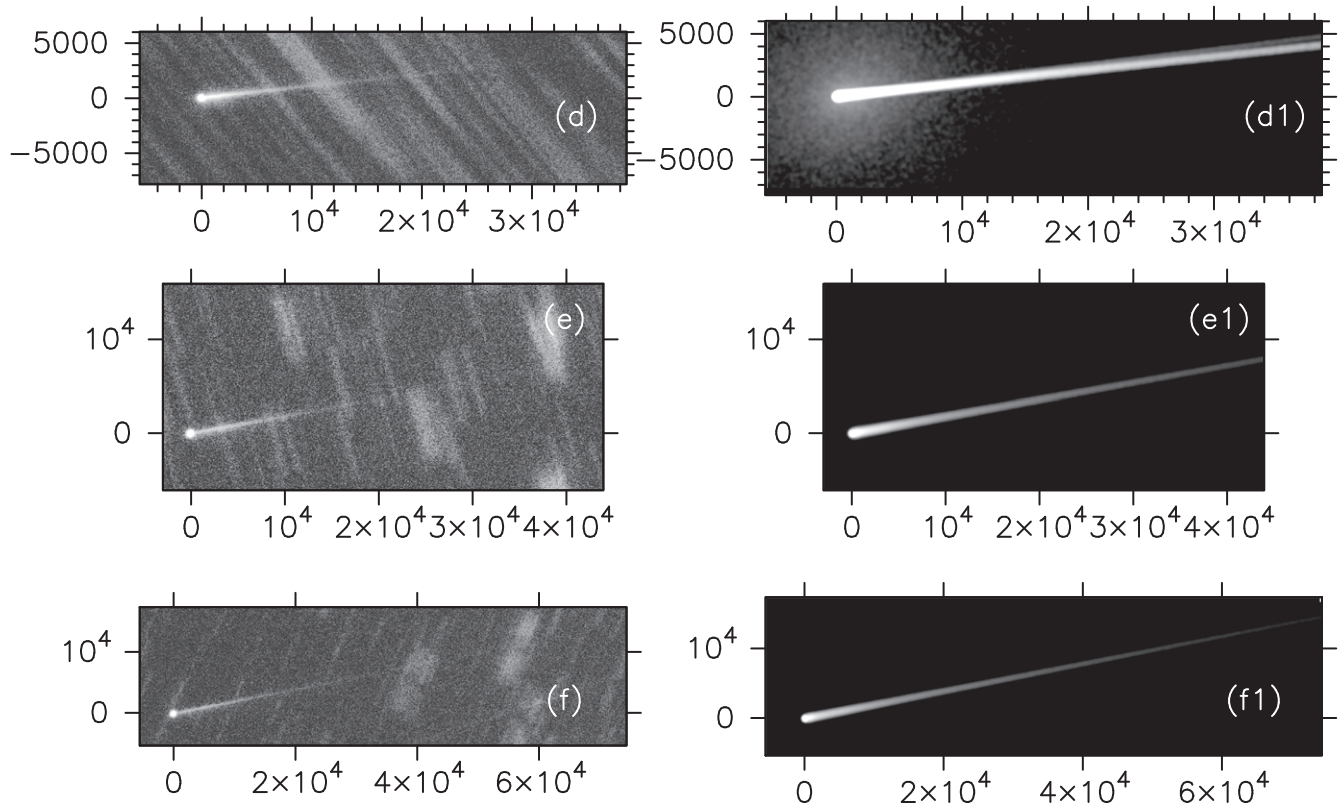


Figure 6. Panels (d), (e), and (f) display the SPACEOBS images at the corresponding dates in Table 2, and panels (d1), (e1), and (f1) display the corresponding synthetic images generated with the simple Monte Carlo model. All images are stretched between 28 and 22 mag arcsec⁻², except synthetic image (d1), which has been heavily stretched between 30 and 25 mag arcsec⁻², barely showing the secondary tail north of the main tail. Axes are labeled in kilometers projected on the sky plane. North is up and east is to the left in all images.

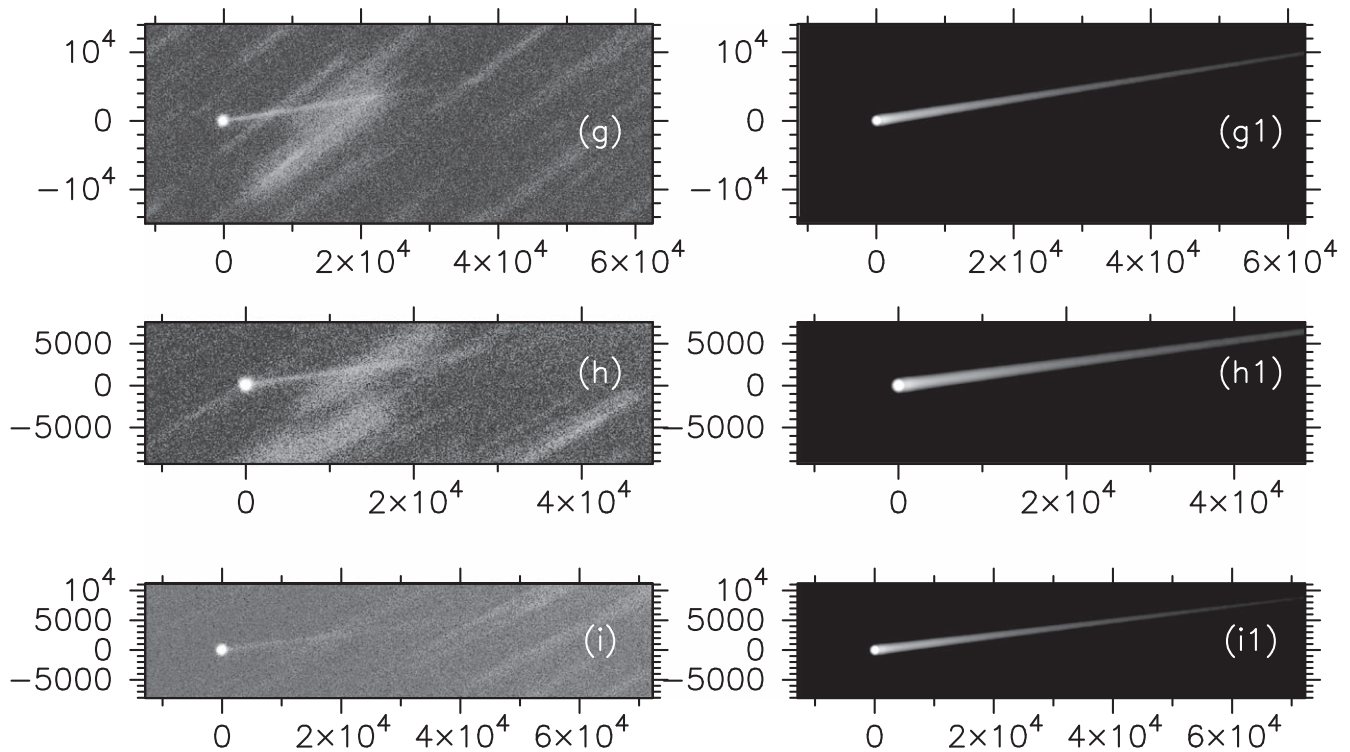


Figure 7. Panels (g), (h), and (i) display the SPACEOBS images at the corresponding dates in Table 2, and panels (g1), (h1), and (i1) display the corresponding synthetic images generated with the simple Monte Carlo model. All images are stretched between 28 and 22 mag arcsec⁻². Axes are labeled in kilometers projected on the sky plane. North is up and east is to the left in all images.

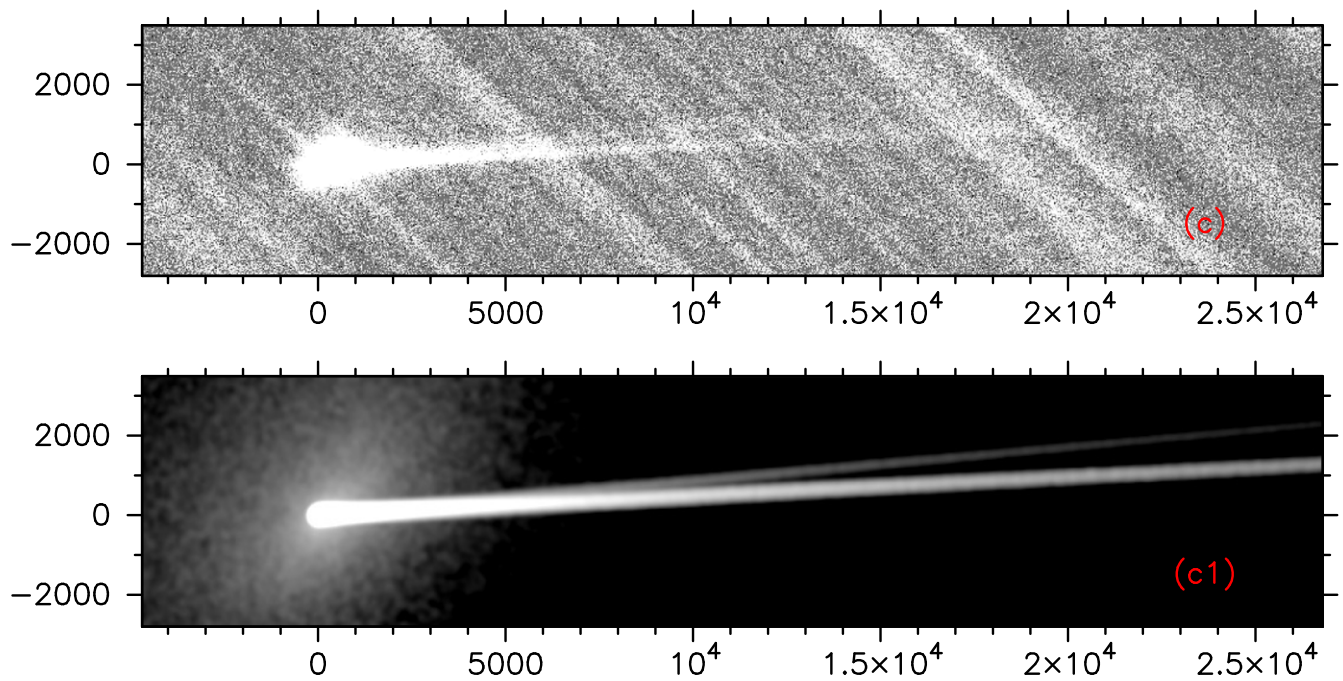


Figure 8. Upper panel: SPACEOBS observation on 2022 October 16 (image labeled (c) in Table 2) of the ejecta barely showing the double tail structure. Lower panel: result of the simple Monte Carlo modeling. Axes are labeled in kilometers projected on the sky plane. North is up, and east is to the left.

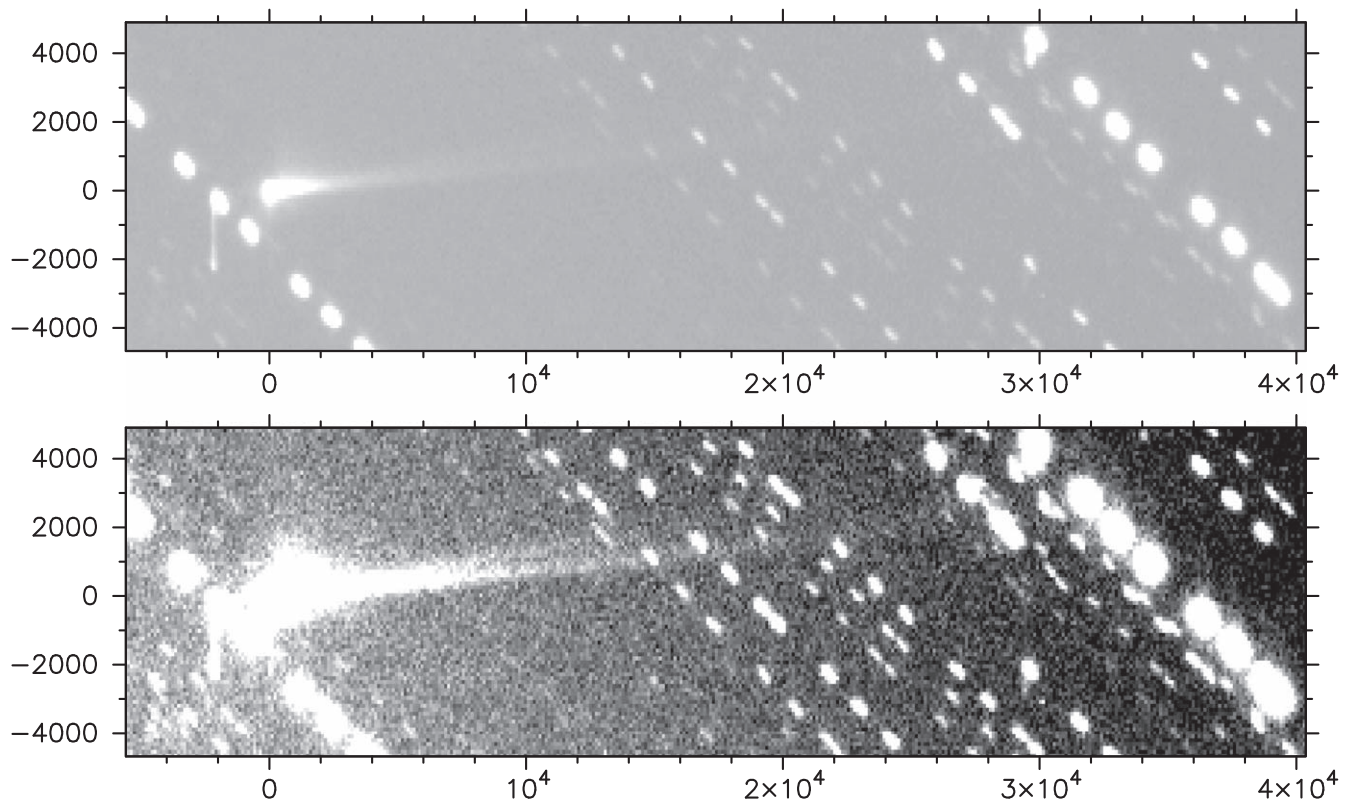


Figure 9. Appearance of the ejecta tail on an image taken at the 1 m telescope of the LULIN Observatory in Taiwan on October 12, 18:19 UT (Lin et al. 2023). The upper panel is the original unstretched image, while the lower panel shows a heavily stretched display to show the double tail structure. Axes are labeled in kilometers projected on the sky plane. North is up, and east is to the left.

image (d) in Table 2, the secondary tail is not seen anymore, although it is still present in the simulations, forming a very small angle with the main tail when the synthetic image is shown heavily stretched (see Figure 6). This is not an effect of

tail vanishing but a geometric effect of the two synchrones associated with the main and secondary events overlapping more and more as the Earth becomes closer to the asteroid orbital plane (see the PIAng column in Table 2).

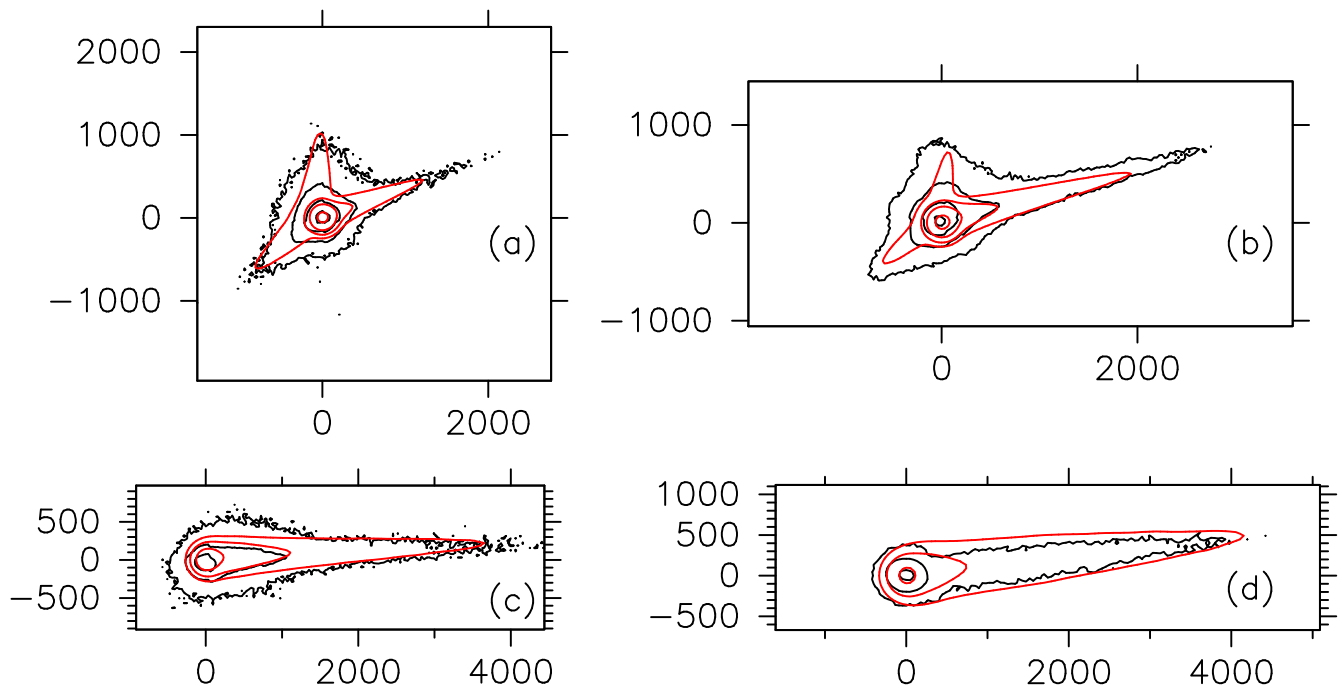


Figure 10. Isophote fields in the innermost regions for the earliest images, (a), (b), (c), and (d) (see Table 2). The observations are represented by black contours and the model by red contours. The isophote levels are 17, 19, 21, and 23 mag arcsec⁻² for images (a) and (b) and 17, 19, and 21 mag arcsec⁻² for images (c) and (d). Axes are labeled in kilometers projected on the sky plane. North is up, and east is to the left in all images.

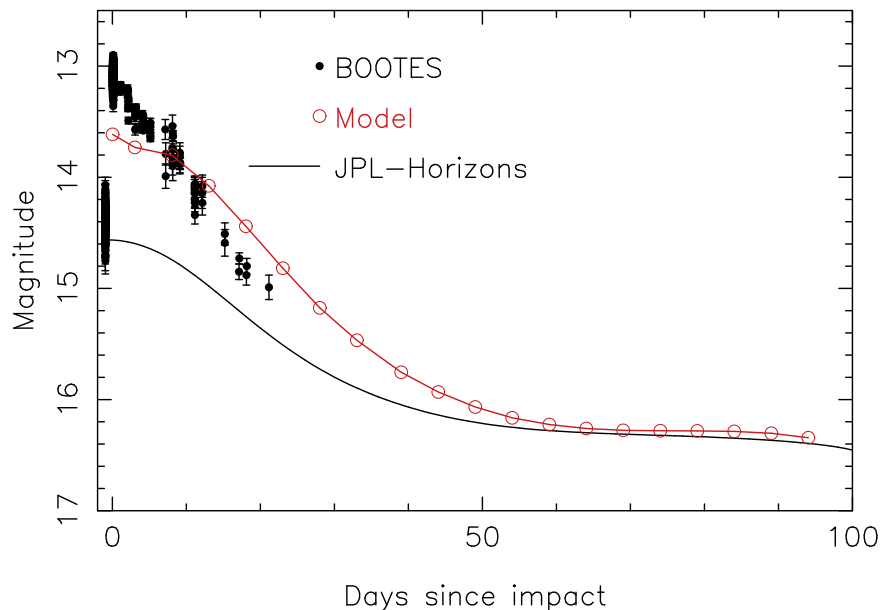


Figure 11. Aperture photometry by BOOTES compared with the simple Monte Carlo model predictions. The solid line is the magnitude as given in the JPL-Horizons system.

A summary of the obtained dust parameters for this simple Monte Carlo model describing the properties of each ejecta component (slow, fast, and late) is given in Table 4.

For the earliest SPACEOBS images, it is useful to build an isophote field to make a detailed comparison with the model. Thus, Figure 10 displays a comparison of the observed and modeled isophotes in the innermost regions close to the maximum condensation. As can be seen, the model fits are quite satisfactory, mostly taking into account the large range in brightness displayed.

Finally, we compare the photometric measurements by BOOTES with the photometry calculated from this model. Figure 11 compares the magnitudes calculated with the model at 5 day intervals since impact and those by BOOTES. The model agrees reasonably well with the measurements. The JPL-Horizons apparent “nuclear” magnitude data are also depicted for comparison at such epochs, which also served to check that the nuclear magnitudes computed with the model nucleus size, geometric albedo, and phase coefficient were correct. The JPL curve is obtained through the IAU H-G system magnitude

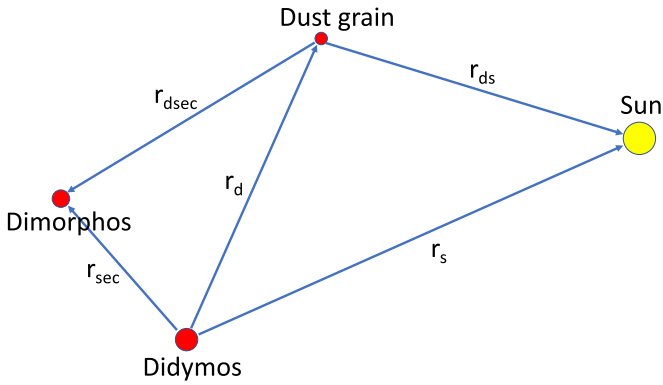


Figure 12. Schematic drawing of the vectors shown in Equation (3).

model with absolute magnitude $H = 18.12$ mag and a G parameter of $G = 0.15$. Our model predicts a small relative maximum near the eighth day after impact, also hinted at by the measurements.

3.2. Detailed Dynamical Monte Carlo Modeling

The visual inspection of the HST images reveals a complex dynamics in the neighborhood of the binary system. Owing to the superb spatial resolution (≈ 2 km pixel $^{-1}$) of the HST WFC3 during the observational time span (see Table 3), a variety of structural details are seen in the images, as has been inventoried by Li et al. (2023). The detailed dynamics of the particles close to the binary components can be described through the integration of the equation of motion of the individual particles subjected to the gravity fields of the two objects, as well as to the solar gravity and radiation pressure. We have already provided the input equations of the model (Moreno et al. 2022a) when performing photometric predictions of the DART impact ejecta. For completeness, we reproduce here the equation of motion of the ejected particles, where the reference frame has its origin in the Didymos center of mass, and the two binary components are assumed to be spherically shaped:

$$\frac{d^2 \mathbf{r}_d}{dt^2} = W_1 \frac{\mathbf{r}_d}{r_d^3} + W_2 \frac{\mathbf{r}_d - \mathbf{r}_s}{\|\mathbf{r}_d - \mathbf{r}_s\|^3} + W_3 \left[\frac{\mathbf{r}_s - \mathbf{r}_d}{\|\mathbf{r}_s - \mathbf{r}_d\|^3} - \frac{\mathbf{r}_s}{r_s^3} \right] + W_4 \left[\frac{\mathbf{r}_{dsec}}{r_{dsec}^3} - \frac{\mathbf{r}_{sec}}{r_{sec}^3} \right], \quad (3)$$

where \mathbf{r}_d is the Didymos-to-dust grain vector, \mathbf{r}_s is the Didymos-to-Sun vector, \mathbf{r}_{dsec} is the vector from the dust grain to Dimorphos, and \mathbf{r}_{sec} is the Didymos-to-Dimorphos vector. We have used the fact that $\mathbf{r}_s = \mathbf{r}_d + \mathbf{r}_{ds}$, where \mathbf{r}_{ds} is the vector from the dust grain to the Sun. Figure 12 provides a schematic drawing of the vectors used. The other terms are $W_1 = -GM_P$, $W_3 = GM_\odot$, and $W_4 = GM_{sec}$, where G is the gravitational constant, M_P is the mass of Didymos, M_{sec} is the mass of Dimorphos, and M_\odot is solar mass. The remaining term, W_2 , is given by

$$W_2 = \frac{Q_{pr} E_s \pi d^2}{c 4\pi 4m_p}. \quad (4)$$

In Equation (4), c is the speed of light, $E_s = 3.93 \times 10^{26}$ W is the total power radiated by the Sun, d is the particle diameter ($d = 2r$), and m_p is the particle mass, $m_p = \rho_p(4/3)\pi r^3$.

As stated in Moreno et al. (2022a), the model has been validated against the MERCURY N -body software package for orbital dynamics (Chambers 1999). The initial conditions are initially assumed in a similar way as in the simple Monte Carlo (see Section 3.1). However, in this more detailed model, the larger particles might spend significant time orbiting the neighborhood of the binary components until either colliding with one of those bodies or leaving the system for interplanetary space (see also Rossi et al. 2022). Therefore, the total mass ejected would actually be larger in this model than was found in the simple model, since a fraction of that mass is lost in collision processes. For the same reason, the velocities of the particles will also have a somewhat different distribution.

We modeled a subset of all of the acquired HST images described in Li et al. (2023). We used the same cone geometry as assumed for the ground-based image modeling and the same size distribution parameters (the same broken power law with the same limiting sizes). We begin by assuming similar values of the total masses ejected and the parameters associated with the velocity distribution. Then, we refine those parameters so as to give the best possible agreement between the model and the observations. As already stated, the fact that this model accounts for the orbital evolution in the neighborhood of the binary components necessarily implies a departure from the parameters obtained above from the relatively more simple model. As before, we considered a double-speed ejecta component released immediately after the impact time and a later secondary ejection event on 2022 October 2.5, the same date as in the simple Monte Carlo model. In order to find a reasonable agreement with the evolution of the brightness and morphology of the observed features, the slow, hemispherical ejecta component had a velocity simply given by $v = v_{esc} = 0.09$ m s $^{-1}$ (where v_{esc} is the Dimorphos escape velocity), while the faster ejecta has $v = 0.225\chi r^{-0.5}$ (where χ is a random number in the (0, 1) interval). The two ejecta components contribute to the ejected mass in the same proportions as assumed in the Monte Carlo simple model. The ejecta speeds differ by factors of less than 2 relative to those found for the simple Monte Carlo model, which is quite reasonable when taking into account the different approaches to the problem.

Regarding the late emission, we assume the same parameters as in the simple Monte Carlo model approach, where this ejection event is characterized by isotropic emission with particle speed $v = v_{esc}$.

The total ejected mass (without taking into account the late emission) from this model is 6.4×10^6 kg, which would be close to the 4.2×10^6 kg estimated using the simple Monte Carlo model considering that a significant fraction of the emitted mass in the detailed model is lost in collisions with either Didymos or Dimorphos.

Concerning those colliding particles, Figure 13 depicts the cumulative dust mass impinging on those surfaces, and Figure 14 displays the total linear momentum transferred to the surfaces of Didymos and Dimorphos per unit time. From Figure 13, we see that for both surfaces, the total masses converge some 20 days after impact to values close to 1.5×10^6 kg. The momentum delivered to Dimorphos (Figure 14) is higher than that on Didymos during the first few hours after impact, but the opposite occurs after ≈ 2 days, where the momentum on Didymos becomes dominant, reaching a maximum ≈ 5 days after impact. This behavior is

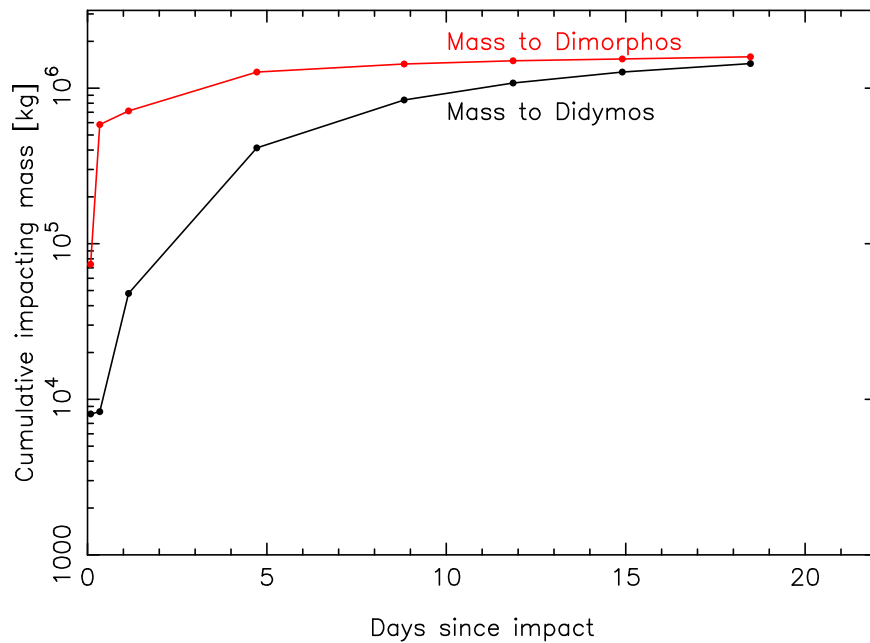


Figure 13. Cumulative impacting dust mass on Didymos and Dimorphos during the 20 days following impact.

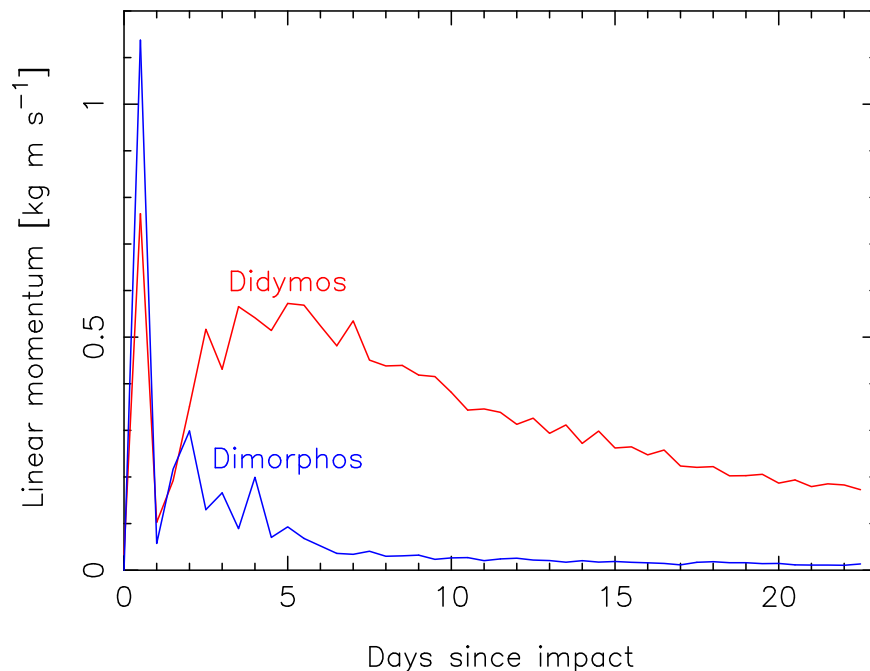


Figure 14. Linear momentum transferred per second to the surfaces of Didymos (red line) and Dimorphos (blue line) as a function of time since the DART impact.

confirmed by what was found by Rossi et al. (2022), where centimeter-sized particles were integrated. The momentum delivered to Didymos becomes dominant several days after the impact up to a time span of tens of days, thanks to particles that evolve within the binary system after being ejected from the impact crater. The reimpact velocities against Didymos are also higher with respect to the ones against Dimorphos, reaching up to 80 cm s^{-1} in the cases analyzed in Rossi et al. (2022). We speculate that this momentum transfer could be the cause of, or at least contribute to, the generation of the secondary tail, as it peaks near the right time, but this argument would need further modeling of the effects of low-speed impacts on the surfaces of

such bodies, which is beyond the scope of this work. In this regard, it should be noted that the secondary tail could also be associated with the dynamical evolution of particles that evolved for a while in the system and then escaped after a few orbits, as revealed by the detailed dynamical analysis performed by F. Ferrari et al. (2023, in preparation).

The total ejected mass agrees very well with that estimated with the simple Monte Carlo model, as the total emission of $6.4 \times 10^6 \text{ kg}$ of particles would actually be reduced to $3.4 \times 10^6 \text{ kg}$ to unbound dust because $\approx 3 \times 10^6 \text{ kg}$ are lost in collisions with the binary components (see Figure 13), leaving close to the $4.2 \times 10^6 \text{ kg}$ of the simple Monte Carlo.

For purposes of comparison, the synthetic images generated are convolved with the HST point-spread function for the appropriate filter and camera used. The HST observations, along with the model images, are shown in Figures 15–17. In Figure 15, the modeled images are heavily stretched to display the antisolar tail extent, which otherwise would be unseen owing to their thinness. The central portion of image (l) and its model (11), along with the isophote fields, is depicted in Figure 18. The outermost modeled isophotes associated with the conical emission are in line with the observations, although the antisolar tail becomes too narrow in comparison with what is observed. On the other hand, the length of the tail constrains the minimum particle radius to $\approx 1 \mu\text{m}$, as assumed in the simple Monte Carlo model; a larger minimum size would result in a too-short tail, and a smaller minimum size would display an incipient tail already on image (j). The secondary tail, which competes in brightness with the main tail, clearly appears in images (o) and (p) (see Figures 16 and 17). This feature had to be modeled by an ejecting dust mass of the order of half of the main event, i.e., $\approx 3 \times 10^6 \text{ kg}$. However, an important fraction of that mass is again reimpacting Didymos and/or Dimorphos, so that only about half of that late mass is released to the interplanetary medium, i.e., $1.5 \times 10^6 \text{ kg}$. This mass is about twice that estimated with the simple Monte Carlo, but since these HST images are far better in resolution than those obtained with SPACEOBS, we prefer to rely on this value. Considering all of the ejected masses, the total contribution to the mass in unbound orbits becomes $4.9 \times 10^6 \text{ kg}$, which agrees fairly well with the value estimated from the simple Monte Carlo model ($4.2 \times 10^6 \text{ kg}$). A summary of the dust properties from the detailed model is given in Table 4.

The photometric measurements on the HST images using a 0.2 aperture (Li et al. 2023) are displayed in Figure 19, together with BOOTES photometry. These two light curves are consistent, showing a constant difference of $0.5 \pm 0.1 \text{ mag}$, owing to the different apertures used. The model results for the subset of HST images shown in Table 3 are found to be in line with the measurements for both data sets.

Although many of the observed features are captured in the model, some of them remain unexplained. Thus, in the early images, the observed tail is broader than the modeled ones, as we have already illustrated in Figure 18. The tail thickness is mostly influenced by the ejection speeds, so that by setting a larger ejection speed, we would get a thicker tail. However, model runs show that while this would work for the earlier images, it would lead to much broader and more diffuse tails than observed for the later images of Figures 16 and 17. On the other hand, while the southern ejecta curtain shows a temporal evolution similar to that retrieved with the model, the northern branch of the ejecta (diffuse ejecta in Figure 2) shows a different evolution with a northeast orientation, while the model predicts a northwest orientation instead, following the direction of the radiation pressure force. In addition, there are also some features in the sunward direction that the model does not reproduce, likely due to the fact that the ejecta cone is asymmetric (Hirabayashi et al. 2023). The origin of such discrepancies is unclear, and many physical parameters are likely contributing. Thus, the model uses spherical particles moving in the gravitational fields of assumed spherical bodies, which is not the case. The dynamics of nonspherical particles in asteroidal or cometary environments is certainly more complex (Ferrari et al. 2017; Ivanovski et al. 2017, 2023; Moreno et al. 2022b), as are the gravitational fields

of nonspherical bodies. On the other hand, the model assumes that the ejected particles have a constant mass and size, excluding any disruption and/or fragmentation processes during their motion. In addition, the ejection pattern is much more complex than described by a simple conical geometry, showing an intricate structure with nonradial filaments (Cheng et al. 2023; Dotto et al. 2023). Future models should incorporate those effects to see how they affect the resulting dust structures in an attempt to understand the physical processes involved.

4. Comparison with Active Asteroids

Active asteroids constitute a recently discovered class of objects in the solar system that, having typical asteroidal orbits, exhibit a comet-like appearance (e.g., Jewitt & Hsieh 2022). The DART mission resulted in the artificial activation of one of these objects, as anticipated by Tancredi et al. (2023), and, following their suggestion, it is interesting to briefly compare the DART results with those observed in naturally activated asteroids. A more extended comparison of the DART results with the natural active asteroids will be the subject of a forthcoming paper (G. Tancredi et al. 2023, in preparation). Following the discovery of 133P/Elst-Pizarro in 1996 (Hsieh et al. 2004), some 40 active asteroids have been detected so far (Jewitt & Hsieh 2022). Among the physical mechanisms that can trigger activation are ice sublimation, rotational destabilization, the result of an impact, or a combination of these. The sample of impacted objects is not statistically significant, as out of that active asteroid population, only four objects have been identified to be most likely activated by an impact with another body, namely, 354P/LINEAR (e.g., Hainaut et al. 2012; Agarwal et al. 2013), (493) Griseldis (Tholen et al. 2015; Jewitt & Hsieh 2022), P/2016 G1 (PAN-STARRS) (Moreno et al. 2016, 2017, 2019; Hainaut et al. 2019), and the large asteroid (596) Scheila (Ishiguro et al. 2011; Moreno et al. 2011). In the case of the DART impact, most of the physical parameters are known in advance: the masses of the impactor and the impacted bodies, the relative velocity, the geometry of the impact, and the impact time. For the natural impacts, none of those parameters are known, not even the collision speed; the relative speed between impactor and impacted body in the DART collision is $\approx 6 \text{ km s}^{-1}$, which is similar to the mean collision speed in the main asteroid belt ($\sim 5 \text{ km s}^{-1}$), but, as pointed out by O'Brien & Sykes (2011), asteroids indeed experience a significant fraction of impacts at velocities much smaller or larger than the “canonical” value. In addition, those naturally impacted objects are normally found to be already active during dedicated sky survey programs such as Pan-STARRS, LINEAR, or the Catalina Sky Survey, and the impact occurred at an unspecified earlier time. In consequence, the evolution of the dust structures cannot be systematically followed as in the DART collision event, where dedicated ground-based and space telescope campaigns have been planned well in advance. Therefore, retrieving information on the dust parameters from scarce data, normally a few images and/or spectra during a short time window, becomes difficult. The determination of the impact time is made through Finson–Probstein or Monte Carlo modeling of the observed tails, but it is always difficult to assess owing to the complex morphology of the observed dust patterns and the large number of dust physical parameters involved. In a way similar to the findings in the DART impact, the resulting particle ejection speeds of the observed ejecta are found to be very small, of the order of the escape velocities of

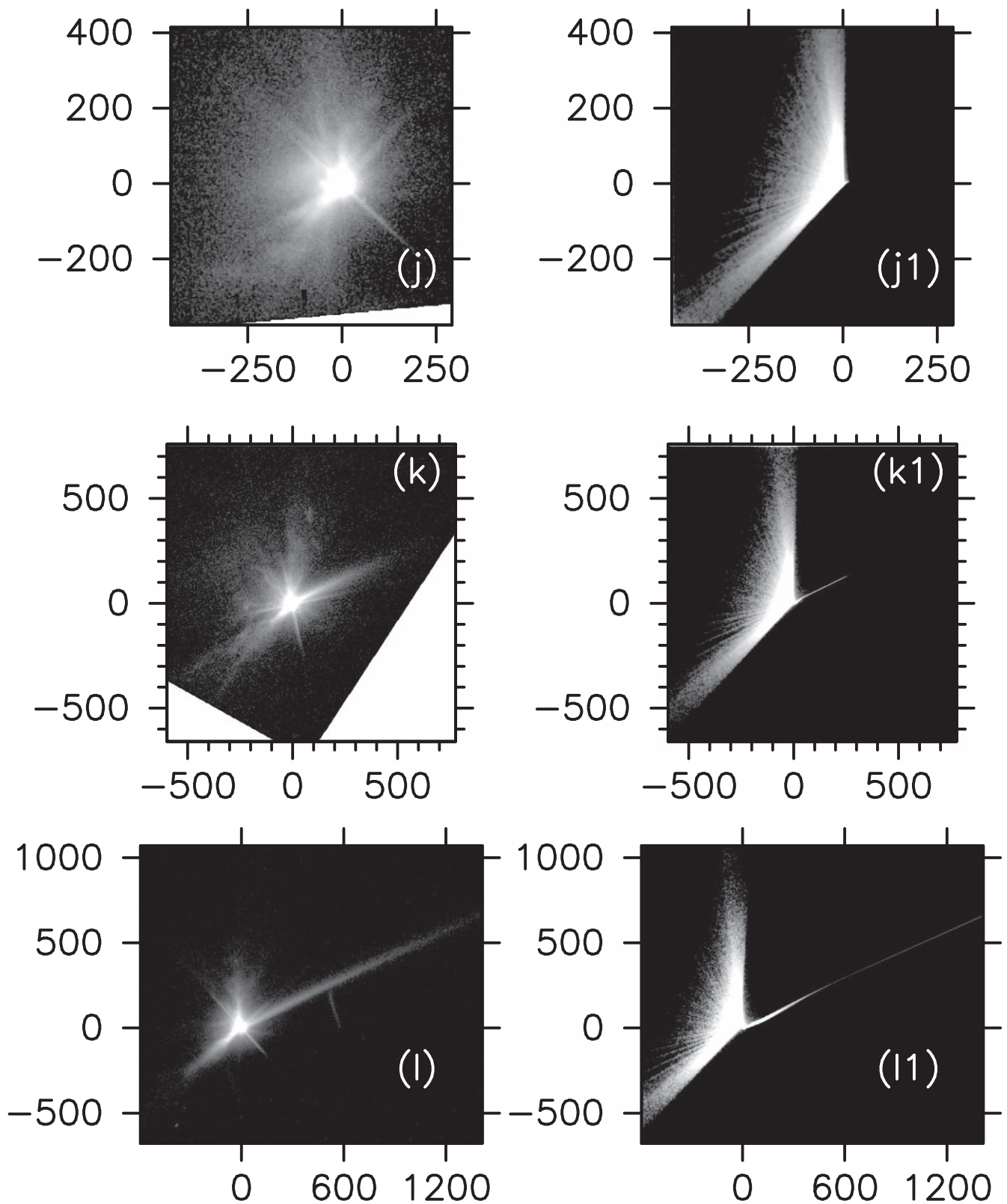


Figure 15. Panels (j), (k), and (l) display HST images on the corresponding dates in Table 3, and panels (j1), (k1), and (l1) display the corresponding synthetic images generated with the detailed Monte Carlo model described in Section 3.2. The HST images are stretched between 22 and 17 mag arcsec⁻² and the modeled ones between 25 and 20 mag arcsec⁻² to show the antisolar tail that would not be seen otherwise because of their thinness. Axes are labeled in kilometers projected on the sky plane. North is up, and east is to the left in all images.

the impacted bodies (e.g., Moreno et al. 2021, and references therein), confirming the scaling law predictions that most of the mass is ejected at low speeds (e.g., Housen et al. 1983).

In contrast, one of the most remarkable differences between the impacted asteroids and Dimorphos is the duration of the observed tails. The fading of the tail on those natural active

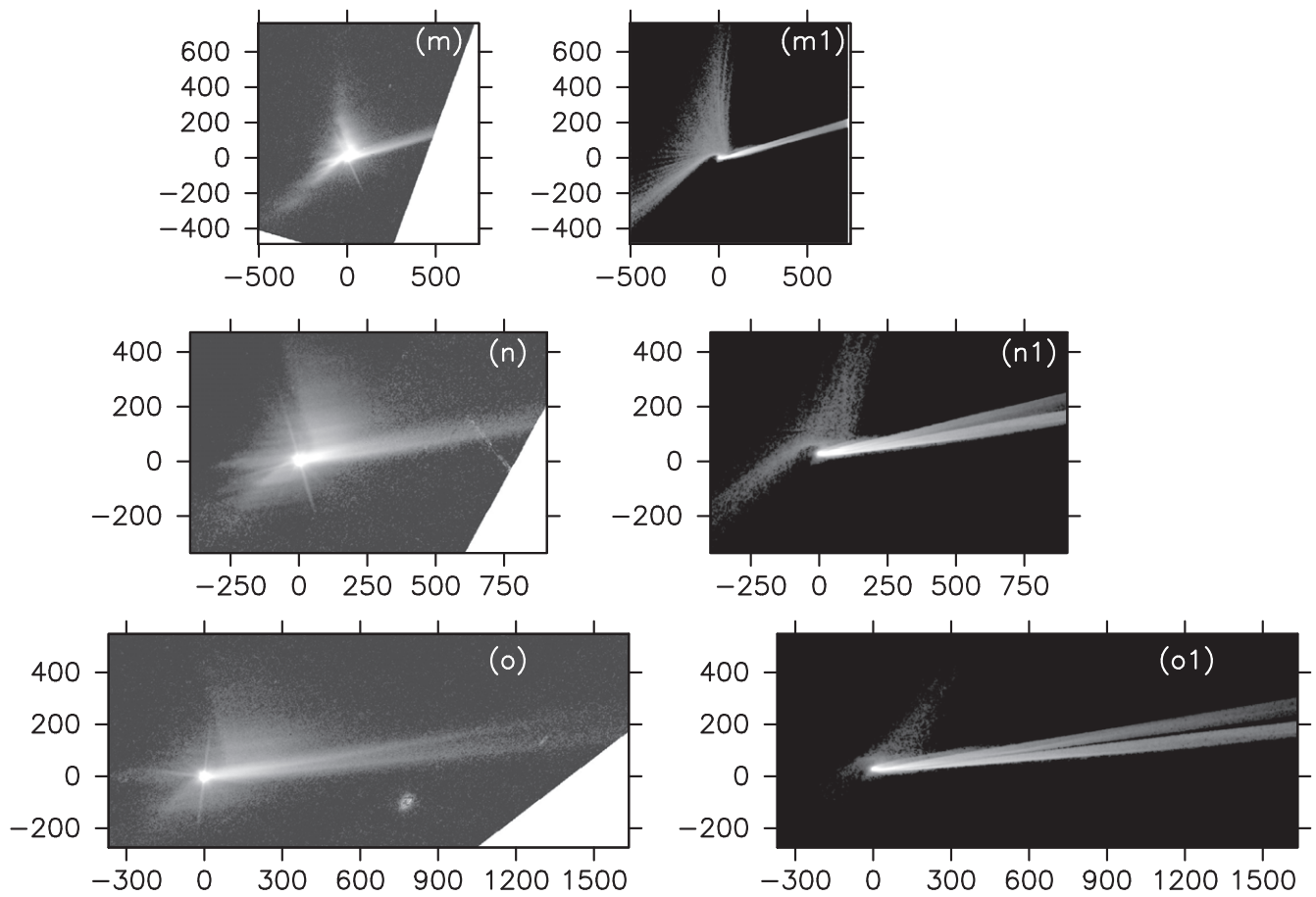


Figure 16. Panels (m), (n), and (o) display HST images on the corresponding dates in Table 3, and panels (m1), (n1), and (o1) display the corresponding synthetic images generated with the detailed Monte Carlo model described in Section 3.2. All images are stretched between 22 and 17 mag arcsec⁻². Axes are labeled in kilometers projected on the sky plane. North is up, and east is to the left in all images.

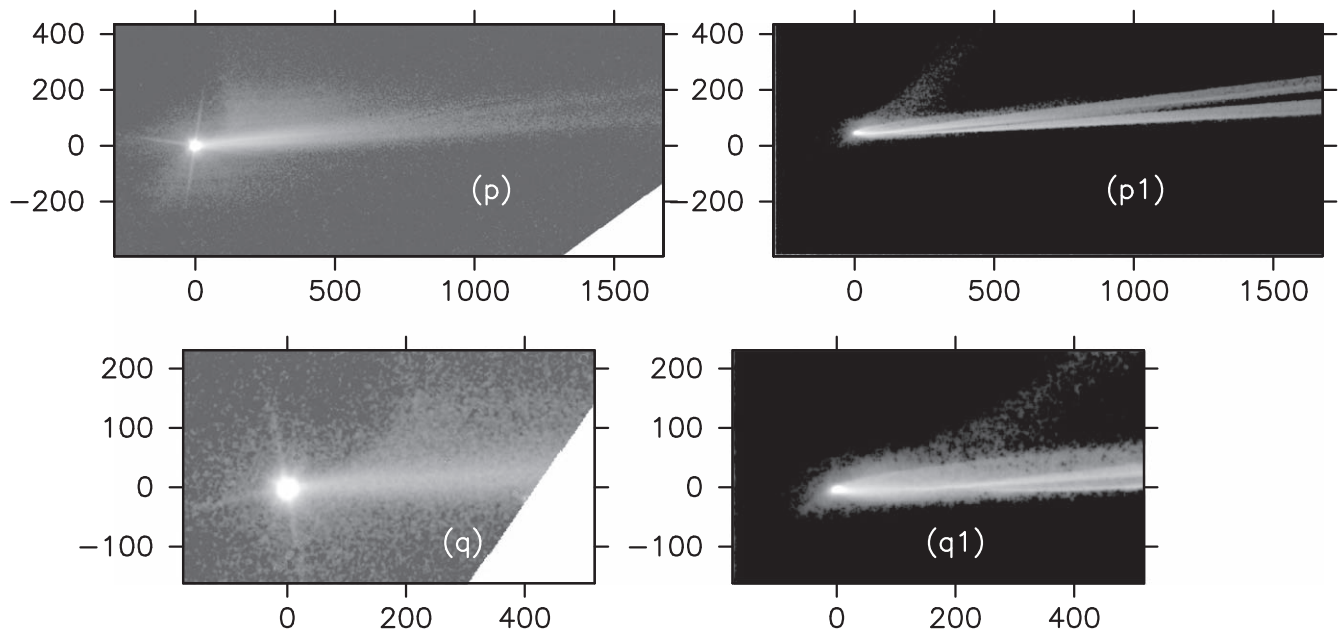


Figure 17. Panels (p) and (q) display HST images on the corresponding dates in Table 3, and panels (p1) and (q1) display the corresponding synthetic images generated with the detailed Monte Carlo model described in Section 3.2. All images are stretched between 22 and 17 mag arcsec⁻². Axes are labeled in kilometers projected on the sky plane. North is up, and east is to the left in all images.

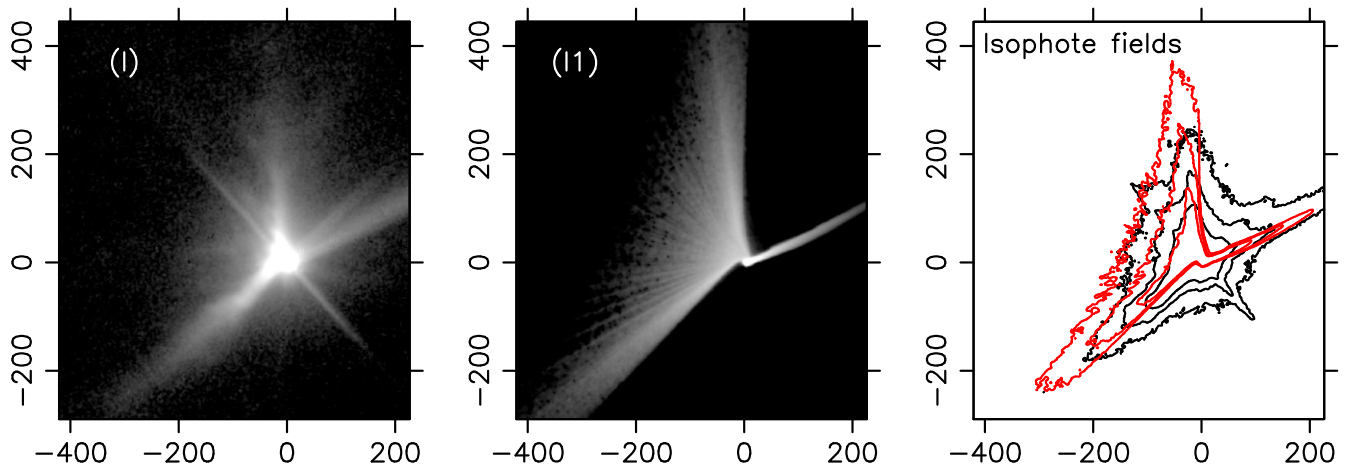


Figure 18. Panel (I) displays the central portion of image (I) (see Table 3), and panel (11) displays the corresponding modeled image. The right panel depicts the isophote fields with contours at 20, 19, and 18 mag arcsec⁻² (black contours correspond to the observation and red contours to the model). All panels are labeled in kilometers projected on the sky and oriented north up, east to the left.

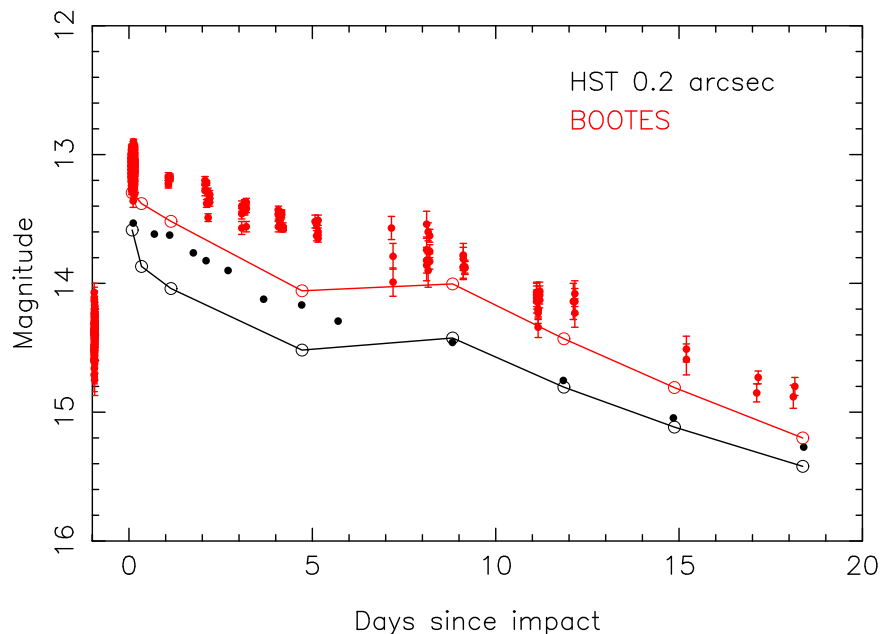


Figure 19. Light curves from HST images with a 0.2'' aperture (Li et al. 2023; black filled circles) compared with BOOTES photometry (with 6''–7'' apertures depending on seeing conditions; red filled circles) and the model results (open circles connected by black and red solid lines for HST and BOOTES, respectively).

asteroids commonly occurs in a time span of several weeks, while the DART tail is still observable more than 9 months after impact (Li et al. 2023). Possibly, the binary nature of the impacted object is playing a role in that long survivability of the tail in keeping relatively large particles orbiting the neighborhood of the binary components for a long time before being ejected to the interplanetary medium. A thoughtful analysis of the long-lasting tail is beyond the scope of this paper.

5. Conclusions

The observed dust ejecta after the collision of the DART spacecraft with Dimorphos, the satellite of the (65803) Didymos system, has been modeled by Monte Carlo dust tail codes. The observations—taken from the Earth and HST, which has the advantage of exploring the ejecta behavior at two different spatial resolutions and spatial scales—are analyzed by simple and detailed Monte Carlo modeling. From the ground-based data

and using our simple Monte Carlo model, we conclude that the differential size distribution of the particles could be represented by a broken power-law function with index $\kappa = -2.5$ for particles between 1 μm and 3 mm and $\kappa = -3.7$ for particles of radii between 3 mm and 5 cm. The ejecta pattern might be explained, on one hand, by particles being ejected along the wall of a hollow cone with its axis pointing to R.A. = 130°, decl. = 17° with relatively large speeds, and on the other hand, by particles emitted hemispherically at Dimorphos's escape speed, oriented in the same way as the emitting cone. With this configuration and an ejected mass of approximately 6×10^6 kg, most of the observed features can be reproduced both morphologically and photometrically at all of the epochs included in the present analysis, keeping in mind that this estimate is always a lower limit, as the presence of large boulders in the distribution, having large mass but contributing negligibly to the brightness, cannot be excluded. The detailed Monte Carlo model takes into account the rigorous motion of the particles in

the neighborhood of the binary system. With this model, various details observed in the ejecta on the HST images have been reproduced, although there remain some that so far cannot be captured with such a model. In any case, the model parameters used to explain the ground-based images can also explain the detailed structures seen in the HST images, in particular, the northern and southeastern streams associated with the hollow cone emission, the early evolution of the ejecta, the length of the antisunward tail, and the double tail pattern. The northern component of the double tail could be associated with reimpacting material on Didymos, as the momentum carried by the impacting particles peaks at nearly the same epoch as that needed to generate the secondary tail. However, further modeling is clearly needed to test this conclusion. There are also many structures readily seen on the HST images, such as the northern diffuse pattern, unreproducible with the model, that needs further modeling including additional processes, such as particle collisions, fragmentation, and disruption phenomena.

Acknowledgments

We are very grateful to the two anonymous referees for their careful reviewing of the manuscript and detailed suggestions, which have helped us to considerably improve the manuscript.

Some of the data presented in this paper were obtained from the Mikulski Archive for Space Telescopes (MAST) at the Space Telescope Science Institute. The specific observations analyzed can be accessed via doi:[10.17909/pvc8-fk24](https://doi.org/10.17909/pvc8-fk24).

F.M. acknowledges financial support from grants PID2021-123370OB-I00 and P18-RT-1854 from Junta de Andalucía and CEX2021-001131-S funded by MCIN/AEI/10.13039/501100011033.

A.C.B. acknowledges funding by the NEO-MAPP project, grant agreement 870377, EC H2020-SPACE-2018-2020/H2020-SPACE-2019.

A.J.C.T. acknowledges support from Spanish MICINN project PID2020-118491GB-I00 and the technical staff at INTA-CEDEA, where the BOOTES-1 station is located.

J.L.O. acknowledges support from contract PID2020-112789GB-I00.

Facilities: HST(STScI), SPACEOBS, BOOTES Global Network, LULIN.

ORCID iDs

Fernando Moreno  <https://orcid.org/0000-0003-0670-356X>

Gonzalo Tancredi  <https://orcid.org/0000-0002-4943-8623>

Alessandro Rossi  <https://orcid.org/0000-0001-9311-2869>

Fabio Ferrari  <https://orcid.org/0000-0001-7537-4996>


Masatoshi Hirabayashi  <https://orcid.org/0000-0002-1821-5689>

Andrew S. Rivkin  <https://orcid.org/0000-0002-9939-9976>

Tony L. Farnham  <https://orcid.org/0000-0002-4767-9861>

Ludmilla Kolokolova  <https://orcid.org/0000-0002-9321-3202>

Javier Licandro  <https://orcid.org/0000-0002-9214-337X>

Jose L. Ortiz  <https://orcid.org/0000-0002-8690-2413>

References

Agarwal, J., Jewitt, D., & Weaver, H. 2013, *ApJ*, 769, 46
Bagnulo, S., Gray, Z., Granvik, M., et al. 2023, *ApJL*, 945, L38

Castro-Tirado, A. J., Jelínek, M., Gorosabel, J., et al. 2012, *Astronomical Soc. of India Conf. Ser.*, Vol. 7, 313
Chambers, J. E. 1999, *MNRAS*, 304, 793
Cheng, A. F., Agrusa, H. F., Barbee, B. W., et al. 2023, *Natur*, 616, 457
Cheng, A. F., Rivkin, A. S., Michel, P., et al. 2018, *P&SS*, 157, 104
Cintala, M. J., Berthoud, L., & Hörz, F. 1999, *M&PS*, 34, 605
Dotto, E., Amoroso, M., Bertini, I., et al. 2023, in *Asteroids, Comets, Meteors Conf. (Flagstaff, AZ)*
Dotto, E., Della Corte, V., Amoroso, M., et al. 2021, *P&SS*, 199, 105185
Dunn, T. L., Burbine, T. H., Bottke, W. F., & Clark, J. P. 2013, *Icar*, 222, 273
Farnham, T., Hirabayashi, M., Deshapriya, P., et al. 2023, in *Asteroids, Comets, Meteors Conf. (Flagstaff, AZ)*
Ferrari, F., Tassora, A., Masarati, P., & Lavagna, M. 2017, *Multibody Physics Dynamics*, 39, 3
Fitzsimmons, A., Berthier, J., Denneau, L., et al. 2023, in *Asteroids, Comets, Meteors Conf. (Flagstaff, AZ)*
Fukugita, M., Ichikawa, T., Gunn, J. E., et al. 1996, *AJ*, 111, 1748
Graykowski, A., Lambert, R. A., Marchis, F., et al. 2023, *Natur*, 616, 461
Hainaut, O. R., Kleyna, J., Sarid, G., et al. 2012, *A&A*, 537, A69
Hainaut, O. R., Kleyna, J. T., Meech, K. J., et al. 2019, *A&A*, 628, A48
Hergenrother, C. W., Maleszewski, C., Li, J. Y., et al. 2020, *JGRE*, 125, e06381
Hirabayashi, M., Farnham, T., Deshapriya, J., et al. 2023, in *Asteroids, Comets, Meteors Conf. (Flagstaff, AZ)*
Housen, K. R., & Holsapple, K. A. 2011, *Icar*, 211, 856
Housen, K. R., Schmidt, R. M., & Holsapple, K. A. 1983, *JGR*, 88, 2485
Hsieh, H. H., Jewitt, D. C., & Fernández, Y. R. 2004, *AJ*, 127, 2997
Hu, Y. D., Fernández-García, E., Caballero-García, M. D., et al. 2023, *FrASS*, 10, 952887
Ieva, S., Mazzotta Epifani, E., Perna, D., et al. 2022, *PSJ*, 3, 183
Ishiguro, M., Hanayama, H., Hasegawa, S., et al. 2011, *ApJL*, 740, L11
Ivanovski, S., Zanotti, G., Bertini, I., et al. 2023, in *Asteroids, Comets, Meteors Conf. (Flagstaff, AZ)*
Ivanovski, S. L., Zakharov, V. V., Della Corte, V., et al. 2017, *Icar*, 282, 333
Ivezić, Ž., Tabachnik, S., Rafikov, R., et al. 2001, *AJ*, 122, 2749
Jewitt, D., & Hsieh, H. H. 2022, arXiv:2203.01397
Kareta, T., Thomas, C., Li, J.-Y., et al. 2023, *NatAs*, submitted
Kim, Y., Ishiguro, M., Michikami, T., & Nakamura, A. M. 2017, *AJ*, 153, 228
Kleyna, J., Hainaut, O. R., & Meech, K. J. 2013, *A&A*, 549, A13
Li, J.-Y., Cheng, A., Chesley, S., et al. 2023, in *Asteroids, Comets, Meteors Conf. (Flagstaff, AZ)*
Li, J.-Y., Hirabayashi, M., Farnham, T. L., et al. 2023, *Natur*, 616, 452
Lin, Z.-Y., Vincent, J. B., & Ip, W.-H. 2023, *A&A*, submitted
Lolachi, R., Glenar, D. A., Stubbs, T. J., & Kolokolova, L. 2023, *PSJ*, 4, 24
Moreno, F., Campo Bagatin, A., Tancredi, G., Liu, P.-Y., & Domínguez, B. 2022a, *MNRAS*, 515, 2178
Moreno, F., Guirado, D., Muñoz, O., et al. 2022b, *MNRAS*, 510, 5142
Moreno, F., Licandro, J., Cabrera-Lavers, A., Morate, D., & Guirado, D. 2021, *MNRAS*, 506, 1733
Moreno, F., Licandro, J., Cabrera-Lavers, A., & Pozuelos, F. J. 2016, *ApJL*, 826, L22
Moreno, F., Licandro, J., Cabrera-Lavers, A., & Pozuelos, F. J. 2019, *ApJL*, 877, L41
Moreno, F., Licandro, J., Mutchler, M., et al. 2017, *AJ*, 154, 248
Moreno, F., Licandro, J., Ortiz, J. L., et al. 2011, *ApJ*, 738, 130
Moreno, F., Pozuelos, F., Aceituno, F., et al. 2012, *ApJ*, 752, 136
Muñoz, O., Moreno, F., Gómez-Martín, J. C., et al. 2020, *ApJS*, 247, 19
Nolan, M. C., Howell, E. S., Scheeres, D. J., et al. 2019, *GeoRL*, 46, 1956
O'Brien, D. P., & Sykes, M. V. 2011, *SSRv*, 163, 41
Okaya, H., Arakawa, M., Yasui, M., et al. 2022, *Icar*, 387, 115212
Opitom, C., Murphy, B., Snodgrass, C., et al. 2023, *A&A*, 671, L11
Oszkiewicz, D., Skiff, B., Warner, B., et al. 2017, in *EPSC, EPSC2017-743*
Rossi, A., Marzari, F., Brucato, J. R., et al. 2022, *PSJ*, 3, 118
Roth, N. X., Milam, S. N., Remijan, A. J., et al. 2023, arXiv:2306.05908
Shestakova, L., Serebryanskiy, A., & Aimanova, G. 2023, *Icar*, 401, 115595
Shevchenko, V. G. 1997, *SoSyR*, 31, 219
Tancredi, G., Liu, P.-Y., Campo-Bagatin, A., Moreno, F., & Domínguez, B. 2023, *MNRAS*, 522, 2403
Tancredi, G., Moreno, F., Campo Bagatin, A., et al. 2023, in *Asteroids, Comets, Meteors Conf. (Flagstaff, AZ)*
Tholen, D. J., Sheppard, S. S., & Trujillo, C. A. 2015, *AAS/DPS Meeting*, 47, 414.03
Weiler, M. 2018, *A&A*, 617, A138
Willmer, C. N. A. 2018, *ApJS*, 236, 47